

Process-model simulations of cloud albedo enhancement by aerosols in the Arctic

Ben Kravitz^{*1}, Hailong Wang¹, Philip J. Rasch¹, Hugh Morrison², and Amy
B. Solomon³

¹Atmospheric Sciences and Global Change Division, Pacific Northwest National Laboratory, Richland, WA.

²Mesoscale and Microscale Meteorology Division, NCAR Earth System Laboratory, National Center for
Atmospheric Research, Boulder, CO.

³University of Colorado Cooperative Institute for Research in Environmental Sciences, NOAA Earth
System Research Laboratory, National Oceanic and Atmospheric Administration, Boulder, CO.

^{*}To whom correspondence should be addressed; P. O. Box 999, MSIN K9-24, Richland, WA 99352, USA;
E-mail: ben.kravitz@pnnl.gov.

1 **Abstract**

2 A cloud-resolving model is used to simulate the effectiveness of Arctic marine cloud bright-
3 ening via injection of cloud condensation nuclei (CCN), either through geoengineering or
4 other increased sources of Arctic aerosols. An updated cloud microphysical scheme is em-
5 ployed, with prognostic CCN and cloud particle numbers in both liquid and mixed-phase
6 marine low clouds. Injection of CCN into the marine boundary layer can delay the collapse
7 of the boundary layer and increase low-cloud albedo. Albedo increases are stronger for pure
8 liquid clouds than mixed-phase clouds. Liquid precipitation can be suppressed by CCN in-
9 jection, whereas ice precipitation (snow) is affected less; thus the effectiveness of brightening
10 mixed-phase clouds is lower than for liquid-only clouds. CCN injection into a clean regime
11 results in a greater albedo increase than injection into a polluted regime, consistent with cur-
12 rent knowledge about aerosol-cloud interactions. Unlike previous studies investigating warm
13 clouds, dynamical changes in circulation due to precipitation changes are small. According
14 to these results, which are dependent upon the representation of ice nucleation processes in
15 the employed microphysical scheme, Arctic geoengineering is unlikely to be effective as the
16 sole means of altering the global radiation budget but could have substantial local radiative
17 effects.

1 Introduction

Aerosol-cloud interactions, including the so-called aerosol indirect effects, are responsible for some of the largest sources of uncertainty in computing the global radiation budget (Boucher *et al.* 2013). The first aerosol indirect effect, also called the cloud albedo effect, refers to the consequences of adding aerosols that act as cloud condensation nuclei (CCN) to clouds under an assumption of fixed liquid water path: CCN may increase the liquid cloud droplet number concentration (CDNC) and thus reduce droplet size, resulting in an increased albedo (Twomey, 1977). The second aerosol indirect effect, also called the cloud lifetime effect, describes how the additional CCN in liquid clouds might change liquid water path causing increases in cloud lifetime, cloud opacity, and areal extent (Albrecht, 1989; Wood, 2012). These aerosol effects are most dramatically seen in marine low clouds, which cover on average 34.0% of the ocean surface (Warren *et al.*, 1988).

Evidence for the aerosol indirect effects can be seen in ship tracks (brighter clouds due to injection of particles from ship plumes; e.g., Radke *et al.*, 1989; Coakley *et al.*, 2000) and in process modeling studies (e.g., Ackerman *et al.* 2003; Wang and Feingold, 2009). Although ship plumes do not always result in brighter clouds (e.g., Chen *et al.*, 2012), this concept in part inspired Latham (1990) to suggest the possibility of deliberately injecting aerosols into the marine boundary layer to increase planetary albedo and cool the planet, counteracting some of the warming effects of anthropogenic greenhouse gas emissions. This proposal is typically known as Marine Cloud Brightening (MCB) and is part of a broader set of strategies called *solar geoengineering*. Due to the ubiquity of marine low clouds, it has been estimated that a 4% increase in global cloud fraction (Randall *et al.*, 1984) or a 6% increase in albedo of existing marine low clouds (Latham *et al.* 2008) could offset atmospheric warming due to a doubling of the CO₂ concentration from preindustrial times. Numerous

42 modeling studies have found that with sufficient, controlled aerosol injection, global warming
43 could be offset, although MCB may not return other fields, like temperature and Arctic sea
44 ice, to their previous levels (e.g., Rasch *et al.*, 2009).

45 Several previous studies have highlighted key points in which microphysical uncertainties
46 have strong influences on the overall uncertainty in the effectiveness of MCB. For example,
47 Pringle *et al.* (2012) showed that achievable CDNC correlates with updraft velocity, ex-
48 plaining in part why the resulting CDNC in simulations by Korhonen *et al.* (2010) were
49 substantially lower than in simulations by Partanen *et al.* (2012), who used more realistic
50 updraft velocities. Many of these microphysical processes operate on the sub-grid scale of
51 global-scale models; process models (such as cloud resolving models) can explicitly resolve
52 the small-scale turbulent updrafts and better represent these microphysical mechanisms that
53 cause some of the uncertainties in global models, providing a useful complement. Wang *et al.*
54 (2011) investigated the effects of MCB in warm marine clouds, revealing the dynamical feed-
55 backs associated with aerosol-induced changes in precipitation and the dependence of MCB
56 effectiveness on meteorological and background aerosol conditions. Jenkins *et al.* (2013)
57 examined the effects of the diurnal cycle on MCB, showing the time of day of injection has a
58 profound impact on aerosol indirect effects; they also found that the aerosol direct effect of
59 scattering solar irradiance can, to some degree, complement the effects of MCB in cloud-free
60 areas. In these two previous process-modeling studies, the injected aerosol particles were as-
61 sumed to be uniformly distributed in the model grid box (a volume on the order of 10^6 m^3)
62 within seconds. Stuart *et al.* (2013) explicitly modeled an aerosol injection plume, showing
63 that due to in-plume aerosol coagulation, the number of aerosols that reach the cloud layer
64 strongly depends upon meteorological conditions.

65 These past process-modeling studies have focused on liquid clouds in a warm marine

66 boundary layer. Doing so spans the vast majority of marine low clouds, but in low tem-
67 peratures, such as in the Arctic, many marine low clouds exist in the mixed phase (i.e., su-
68 percooled liquid droplets and ice particles coexist). Cloud microphysical processes in clouds
69 that contain ice, and hence the mechanisms that drive aerosol-cloud interactions, are differ-
70 ent from the processes in warm marine clouds (see Section 2.2 below). Interactions between
71 ice particles and liquid drops add additional levels of complexity to the aerosol effects (e.g.,
72 Morrison *et al.*, 2012). As such, a set of questions could be asked about the effectiveness of
73 MCB in ice-containing clouds in cold environments; such questions clearly have relevance for
74 future climate. For example, increasing the shortwave reflectivity of the Arctic could offset
75 some of the effects of reduced Arctic albedo due to receding sea ice. Moreover, if sufficient
76 portions of the Arctic ocean become ice-free, Arctic shipping could increase, and hence the
77 presence of ship tracks could be more prevalent. These effects could be counterbalanced by
78 the longwave impacts of mixed-phase clouds, which are known to dominate cloud radiative
79 effects in the Arctic (Morrison *et al.* 2012).

80 In this study, we use a cloud resolving model to assess some of the effects of introducing
81 CCN into marine low clouds in the Arctic from a single point source representing a ship.
82 This is one of the proposed methods in MCB of introducing CCN into marine low clouds.
83 In particular, we address the following questions throughout the course of this paper:

- 84 1. According to our model simulations, does CCN injection in the Arctic increase low-
85 cloud albedo?
- 86 2. Are the albedo effects of aerosol-cloud interactions stronger for supercooled liquid or
87 mixed-phase clouds?
- 88 3. Is there a difference in albedo effects between injection of CCN into a clean environment

89 versus a polluted one?

90 **2 Model and Methods**

91 **2.1 Model Setup**

92 Our simulations are conducted using the Advanced Research Weather Research and Fore-
93 casting (WRF) model (Version 3.3; Skamarock *et al.* 2008), used as a cloud-resolving model.
94 Third-order Runge-Kutta time stepping is applied to the dynamics. Fifth and third order ad-
95 vection is employed in the horizontal and vertical directions, respectively, with a monotonic
96 limiter applied to the time integration scheme; this advection scheme is particularly impor-
97 tant for the transport of tracers (Wang *et al.* 2009). The fine-resolution WRF model has been
98 used in process-modeling studies of warm clouds and mixed-phase clouds and compared with
99 other models participating in intercomparison cases (e.g., Wang *et al.* 2009; Ovchinnikov *et*
100 *al.* 2014). It has proven to be a useful tool for studying aerosol-cloud interactions.

101 We use a modified version of the setup of the model intercomparison based on the Indirect
102 and Semi-Direct Aerosol Campaign (ISDAC; McFarquhar *et al.* 2011; Ovchinnikov *et al.*
103 2014). The initial profile for our simulations is given in Table 1; the temperature and
104 specific humidity in the free troposphere (altitudes above 1200 m) are nudged (Newtonian
105 relaxation) toward this initial profile with a time scale of one hour, and winds at all levels
106 are nudged with a time scale of two hours. This is accomplished by adding an unphysical
107 tendency term to all of the nudged fields with a height-dependent maximum magnitude of
108 $\Delta t \Delta \phi / (1 \text{ hour})$ or $\Delta t \Delta \phi / (2 \text{ hours})$, respectively, where Δt is the model timestep of three
109 seconds, and $\Delta \phi$ is the departure of the nudged field from the initial profile. The initial
110 profile is characterized by an inversion at 825 m altitude and supersaturated conditions so

111 a cloud forms underneath the inversion level immediately after the simulation starts. This
112 is a common setup for model intercomparisons of Arctic mixed phase clouds (Klein *et al.*,
113 2009; Morrison *et al.*, 2011; Ovchinnikov *et al.*, 2014), all of which were based on observed
114 temperature and humidity profiles. Ovchinnikov *et al.* 2014 specified nonzero wind shear
115 in the initial meteorological profile, but this study specifies no initial wind shear so as not
116 to further complicate detection of signals in our output; turbulence-induced wind shear is
117 allowed to develop over the course of the simulation. The implications of this modification
118 are discussed in Section 4. The surface pressure is specified to be 1020 mb, and the surface
119 skin temperature is 267 K. The surface roughness length is 0.004 m (Morrison *et al.* 2011).
120 Large-scale air subsidence is calculated by vertical integration of a specified horizontal wind
121 divergence ($5 \times 10^{-6} \text{ s}^{-1}$) from the surface to the inversion, with zero divergence above the
122 inversion, and is applied to temperature and humidity. Sensible and latent heat fluxes at
123 the surface are set to zero for the entire simulation. The choices of no heat and moisture
124 surface fluxes were to reduce the number of sources of externally-driven variability in model
125 behavior. These values can be compared to observed values of sensible and latent heat
126 fluxes of -2.07 and -5.09 W m^{-2} , respectively, taken during August 2001 over a region of
127 drifting pack ice (Birch *et al.* 2009). The implications of these choices are discussed in
128 Section 4. A sensitivity study to explore different values of surface heat fluxes will be
129 undertaken in the future. As is typical in process-model simulations, the domain is doubly
130 periodic in the horizontal directions, without advective forcing for heat and moisture in
131 the domain, although the nudging provides a source term for temperature and humidity to
132 prevent significant drift in the environmental conditions. We include both shortwave and
133 longwave radiation schemes (CAMRT; Collins *et al.* 2006). The boundary-layer turbulence is
134 initiated via a small random perturbation to the temperature field. The 1.5 order turbulent

135 kinetic energy (TKE) closure is used to calculate subgrid-scale diffusion (Deardorff 1972).

136 The model domain is 120 km in the x direction (400 grid cells, each 300 m in size), 60
137 km in the y direction (200 grid cells, each 300 m in size), and 1.5 km in the z direction
138 (50 layers, each approximately 30 m thick). This is the same domain size used by Wang
139 *et al.* (2011). The location of the domain is 71.32°N , 156.61°W , which is relevant only for
140 shortwave radiative flux calculations. At this latitude, our model domain covers an area that
141 is approximately equivalent to a single grid box corresponding to the current resolution of
142 many global models.

143 **2.2 Microphysical Parameterizations**

144 A two-moment bulk microphysics scheme based on Morrison *et al.* (2005, 2009) is used
145 in all model simulations. Some simulations have the ice processes switched off to focus on
146 pure supercooled liquid clouds (Table 2). This scheme is one of the microphysical options
147 in the WRF model; however, we have modified the default scheme for this study, mostly to
148 accommodate the injection of aerosols from a moving point source. A prognostic variable for
149 interstitial accumulation-mode aerosol number concentration has been added, as was done
150 by Wang *et al.* (2009) for a different microphysical scheme. Droplet activation was pa-
151 rameterized following Abdul-Razzak and Ghan (2000) as a function of the vertical velocity,
152 temperature, pressure, and aerosol size distribution parameters. Sub-grid scale vertical ve-
153 locity is not parameterized, and all vertical velocities are calculated at the grid scale, which
154 could potentially lead to underprediction of the number of cloud droplets that are activated.
155 Aerosol particles are incorporated into liquid drops upon activation (i.e., a sink of particle
156 number) and returned to the interstitial state after drop evaporation (i.e., a source of particle
157 number) in any given grid box. It is assumed that each evaporated liquid drop releases one

158 single aerosol particle (Feingold *et al.* 1996; Mitra *et al.* 1992), indicating that drop coales-
159 cence acts as a removal process for aerosol particle number in addition to the sedimentation
160 and ultimate loss of larger drops to the surface. Scavenging processes considered in the
161 model simulations include nucleation scavenging, collision/coalescence, resuspension, and
162 wet deposition; collision/coalescence and wet deposition directly reduce total CCN number
163 concentration in the boundary layer. The present study includes heterogeneous nucleation
164 from cloud droplet freezing, which is one major difference from the SHEBA and ISDAC
165 intercomparisons (Morrison *et al.* 2011; Ovchinnikov *et al.* 2014).

166 The microphysical scheme uses a lognormal size distribution with a fixed modal radius of
167 $0.1 \mu\text{m}$ and a geometric standard deviation of 1.5 to represent accumulation-mode aerosols.
168 Therefore, the injected and resuspended aerosols do not modify the particle sizes and spec-
169 trum width. For simplicity, the coarse-mode aerosol is also switched off for all simulations.
170 Ice nucleation through contact and immersion freezing of cloud droplets and immersion
171 freezing of rain drops is included in the model. The effective diffusivity of contact ice nu-
172 clei, assuming a size of $0.1 \mu\text{m}$, is based on Morrison and Pinto (2005). Immersion freezing
173 of cloud droplets and rain drops follows the drop-volume dependent parameterization of
174 Bigg (1953). In conditions of temperature less than -8°C and water saturation or ice super-
175 saturation greater than 8%, deposition and condensation freezing nucleation processes are
176 represented by a relaxation of the cloud ice number concentration to 0.16 L^{-1} if the existing
177 total ice (cloud ice, snow, and graupel) concentration falls below this value in one model
178 time step.

179 For the purposes of activation into cloud droplets, aerosols are assumed to have the
180 same properties as ammonium sulfate aerosols. Because these are the only aerosols consid-
181 ered in this study, and because ammonium sulfate aerosols are efficient CCN, we use the

182 terms aerosol and CCN interchangeably. We discuss the implications of this assumption in
183 Section 4.

184 **2.3 Simulation Design**

185 We perform a suite of eight simulations, each lasting 30 hours, starting at 6 p.m. on 26
186 April and ending at 12 a.m. on 28 April (local time). In these simulations, we specify
187 the background concentration of CCN, whether the ice processes were included or excluded,
188 and whether CCN injection was included or excluded. Table 2 details the eight different
189 simulations, as well as the naming conventions for each experiment. The “clean” case is
190 considered to have an initial background CCN of 50 cm^{-3} , and the “polluted” case to have
191 an initial background CCN of 200 cm^{-3} , consistent with global mean values (Latham, 2012).
192 These values are also consistent with measurements taken in the Arctic. During the Mixed
193 Phase Arctic Cloud Experiment (M-PACE; Verlinde *et al.* 2009), background CCN was
194 measured to be approximately 40 cm^{-3} , and during SHEBA/FIRE-ACE, the background
195 was approximately 200 cm^{-3} (Curry *et al.* 2000; Fridlind *et al.* 2012).

196 Wang *et al.* (2011) included a uniform background source of CCN of $2 \text{ mg}^{-1} \text{ h}^{-1}$ in
197 each grid box within the boundary layer to account for natural sea-salt emissions. This
198 source term was also used to balance the loss of CCN due to coalescence of cloud drops and
199 subsequent wet removal that may result in a super-clean collapsed boundary layer (Ackerman
200 *et al.* 1993; Wang *et al.* 2010). In the current study, we did not include such a background
201 source, as we were interested in diagnosing the ability of CCN injection to prevent the
202 boundary layer from collapsing. Low CCN conditions that are incapable of sustaining a
203 boundary layer structure have been observed in nature (Ackerman *et al.* 1993), so although
204 such conditions are not necessarily ubiquitous, our simulation design is relevant to potential

205 real-world conditions.

206 To simulate particle injection, we follow the method of Wang *et al.* (2011). From the
207 beginning of the simulation, CCN are emitted into the lowest atmospheric layer from a
208 single moving point source (one grid box in size), representing injection from a ship. This
209 design is equally applicable for both deliberate CCN injection (MCB) or emissions from
210 cargo shipping. The CCN emission rate is $1.45 \times 10^6 \text{ m}^{-2} \text{ s}^{-1}$ from a point source moving at
211 5 m s^{-1} , where the point source begins at the West side of the domain and travels Eastward;
212 then because the domain is doubly periodic, the point source re-appears at the West side
213 of the domain after it passes the East border and continues to emit particles, traveling
214 Eastward. This emission rate of the total number of particles injected to the atmosphere is
215 the same as suggested by Salter *et al.* (2008) for geoengineering purposes, except that the
216 injected CCN take the same lognormal size distribution as the background aerosols rather
217 than a uniform size. We did not consider the potential for in-plume aerosol coagulation
218 (Stuart *et al.* 2013), instead implicitly assuming a sufficient amount of particles are injected
219 to achieve the mass loading used in this study. The aerosol particles have composition
220 properties corresponding to ammonium sulfate. Further investigations could explore the
221 effects of particle composition on our results; we discuss some of the implications of this
222 assumption in Section 4. CCN number is reported as two separate prognostic variables:
223 the “active” CCN number is calculated based on full interactivity with cloud scavenging
224 processes, and the “passive” CCN number does not include scavenging within clouds.

225 In all simulations of mixed-phase clouds, the ice processes were not included until two
226 hours after the beginning of the simulations. This is consistent with the ISDAC model
227 intercomparison; this specification was included to allow the boundary-layer turbulence to
228 develop before the ice processes kick in (Ovchinnikov *et al.* 2014).

229 All reported values of liquid water path were calculated using cloud water only. Inclusion
230 of rain in these calculations has negligible impacts on values of liquid water path. Conversely,
231 as is shown in the following section, most of the ice in these simulations is in the form of
232 snow, so all calculations of ice water path include ice crystals, snow, and graupel.

233 In Section 3.2, there is a discussion of cloud fraction. For the purpose of this calculation,
234 a grid box is said to have liquid cloud if the cloud liquid water mixing ratio is at least 0.01 g
235 kg^{-1} . A grid box has ice cloud if the ice water mixing ratio is at least $10^{-5} \text{ g kg}^{-1}$. Column
236 cloud fraction is defined as the fraction of all model columns in which cloud optical thickness
237 is at least 2.

238 **3 Results**

239 We begin our investigation of marine cloud brightening in Section 3.1 with a discussion of
240 the injected particles, their transport, and their activation into cloud droplets. Section 3.2
241 explores changes in the clouds as a result of injection, including cloud fraction, cloud albedo,
242 and cloud depth. Finally, Section 3.3 explores the susceptibility of the clouds to brightening.

243 **3.1 Particle Injection and Activation**

244 Although our setup was different from the specifications given by Ovchinnikov *et al.* (2014)
245 for the ISDAC intercomparison, we nevertheless find it useful to contextualize results from
246 our non-injection simulations through a comparison with the results from that study. One
247 major difference between our simulations and those of Ovchinnikov *et al.* (2014) is that in
248 lieu of the complex ice particle activation scheme employed in our simulations, Ovchinnikov

249 *et al.* (2014) prescribed the ice nucleation rate to be

$$\left\{ \begin{array}{ll} \frac{\partial N_i}{\partial t} = \max\left(0, \frac{N_{i_0} - N_i}{\Delta t}\right) & S_i \geq 0.05 \text{ or } q_i \geq 0.001 \text{ g kg}^{-1} \\ 0 & \text{otherwise} \end{array} \right. \quad (1)$$

250 where N_i is ice crystal number, S_i is the supersaturation fraction, and q_i is the liquid water
 251 mixing ratio. N_{i_0} is a prescribed target ice particle concentration; simulations were conducted
 252 for which $N_{i_0}=0, 1, \text{ or } 4 \text{ L}^{-1}$. Within the first eight hours of simulation (the duration of
 253 simulations described by Ovchinnikov *et al.*, 2014), the liquid-only simulations in this study
 254 have similar liquid water paths to the $N_{i_0}=0 \text{ L}^{-1}$ case (Figure 1c). Inclusion of ice processes
 255 yields liquid and ice water paths similar to $N_{i_0} = 1 \text{ L}^{-1}$ (Figure 1d). The liquid and ice
 256 water paths depicted in Figure 1 of the present study show greater spread after 12 hours of
 257 simulation, approximately incident with sunrise, so we are unable to definitively state that
 258 the results presented here exactly replicate a particular simulation described by Ovchinnikov
 259 *et al.* (2014). Moreover, the simulations in the ISDAC intercomparison were only performed
 260 for night times, so we do not know whether differences between simulations in the calculated
 261 liquid and ice water paths begin to grow larger due to the inclusion of diurnal variation or
 262 whether this divergence is simply due to a sufficiently long simulation time.

263 The idea of MCB hinges on the injected CCN activating into cloud droplets. CCN
 264 injection clearly results in an increase in CDNC (Figures 1a and 3a). In the absence of
 265 injection, the boundary layer collapses (i.e., cloud top decreases; Figures 2b and 4b) and
 266 clouds dissipate, coincident with a rapidly declining CDNC to $1\text{-}2 \text{ cm}^{-3}$ by the end of the
 267 simulations. The decreasing trend of CDNC shows little dependence on whether ice processes
 268 are included, nor whether the background is clean or polluted. Despite having no sensible
 269 or latent heat fluxes at the surface, CDNC increases in the injection simulations, showing

270 that the boundary-layer turbulence, driven primarily by cloud radiative cooling, is sufficient
 271 to loft the injected particles from the surface into the cloud within about three hours.

272 The plots of CDNC show an oscillatory pattern for the injection simulations but not
 273 the no-injection simulations. This oscillation is likely in part due to the CCN point-source
 274 traversing the periodic domain repeatedly, which has a period of approximately 7 hours;
 275 CDNC values reach a dynamic balance between additional injection of CCN and scavenging
 276 of CCN via activation, collision/coalescence, and resuspension. There are additional oscil-
 277 lations with a period of approximately 3 hours. These could be due to local precipitation-
 278 dynamical interactions, or they could be related to the eddy turnover time in the decoupled
 279 boundary layer, but we are as of yet unable to attribute these oscillations to a particular
 280 mechanism.

281 Figure 5 shows transport efficiency, which we define as

$$\text{TE} = \frac{N_P - B}{N_P^{\text{surf}} - B} \quad (2)$$

282 where N_P is the number concentration of the passive tracer at each level, N_P^{surf} is the number
 283 concentration of the passive tracer at the level of injection (the lowest model layer), and B is
 284 the background concentration of particles (either 50 or 200 cm^{-3}). This quantity indicates
 285 how efficiently the injected particles are transported from the surface layer to other model
 286 layers in the absence of cloud scavenging processes. All simulations show very efficient
 287 transport at or below the cloud layer, in some cases exceeding 95%. In the second half of the
 288 simulation, some of the aerosol is transported into the free troposphere above the boundary
 289 layer top.

290 The sudden jump in TE within the first few hours of simulation (Figure 5) could be due
 291 to a transition from the initial part of the simulation, in which the cloud layer is decoupled

292 from the sub-cloud layer, to a state in which vertical transport from the surface to the
 293 cloud layer is stronger due to increased coupling. To ascertain the mechanisms behind this
 294 transition, Figure 6 shows the buoyancy flux of turbulence and the variances of the vertical
 295 velocity (σ_w^2) for all simulations. A decoupled system is sometimes characterized by negative
 296 buoyancy flux near the cloud base and a cloud-base minimum in σ_w^2 (Stevens *et al.* 2005);
 297 both of these features are seen early in the simulations. However, all simulations undergo
 298 a transition from negative buoyancy flux at the surface to near-neutral buoyancy flux and
 299 from $\sigma_w^2 \approx 0$ at the surface to slightly positive values. Moreover, buoyancy fluxes and σ_w^2
 300 values transition away from features indicating a de-coupled state to a more strongly coupled
 301 state. This suggests that there is sufficient vertical motion to transport the aerosols up into
 302 the cloud layer despite the lack of surface heat and moisture fluxes.

303 The scavenging efficiency (Figures 2a and 4a) is defined here as

$$SE = 1 - \frac{N_T}{N_P^{\text{cloud}}} \quad (3)$$

304 where N_T is the total number of cloud droplets (CDNC) plus the number of interstitial
 305 CCN, and N_P^{cloud} is the number concentration of the passive tracer that is in cloudy grid
 306 cells. Because N_T is affected by scavenging processes, but N_P is not, the quantity SE gives an
 307 indication of how efficiently the scavenging processes (collision/coalescence and precipitation)
 308 are operating to reduce the number of CCN. SE values increase over the course of the
 309 simulations due to scavenging of existing particles via precipitation (Figures 2c-d, 4c-d, and
 310 10) or collision/coalescence; both of these processes reduce N_T . Figures 1e-f and 3e-f show
 311 that droplet size increases before the collapse of the boundary layer (formal definitions of
 312 cloud droplet effective radius as calculated in this study are given in Section 3.2); this is
 313 concurrent with increases in LWP and/or decreases in CDNC, indicating a combination of

314 growth of existing particles and collision/coalescence. Figures 2a and 4a show that SE is
315 lower for all injection simulations, indicating two main effects. The dominant effect of CCN
316 injection is to provide new particles for activation into cloud droplets, thus reducing SE. A
317 secondary effect is to increase the number of interstitial aerosols, thus increasing N_T .

318 SE values show almost no dependence upon whether ice processes are included in the
319 simulations, which is perhaps not surprising, as only a small fraction of droplets freeze and
320 form ice. In the no-injection cases, the background CCN number has little effect on SE.
321 However, injection into a relatively clean environment results in a lower SE than injection
322 into a polluted environment. Figures 1e and 3e show that injection into a clean regime
323 results in a lower cloud droplet size; smaller droplets have lower collection efficiencies, which
324 would contribute to a lower SE than in the no-injection simulations.

325 Wang and Feingold (2009) and Wang *et al.* (2011) showed that reduced precipitation
326 along the ship plume can induce dynamical feedbacks that lead to moist convergent flow
327 into the ship track, thickening clouds along the track but thinning the neighboring off-track
328 clouds. The thickened clouds eventually produce stronger precipitation, counteracting the
329 aerosol indirect effects. Likely due to the dry conditions, low liquid water paths (Figures
330 1c and 3c), and a more stable boundary layer in the Arctic than in the subtropical marine
331 boundary layer, the dominant modifications to cloud properties here can be explained by
332 the conventional aerosol indirect effects, without the additional complications of dynamical
333 effects due to precipitation. There are some dynamical circulation changes due to precipita-
334 tion, as is evident from the oscillation period discussed in Section 3.1, but the net effects on
335 clouds are small.

336 Figure 7 gives the spatio-temporal distribution of the injected particle concentration. The
337 off-track parts of the domain give an indication of behavior in the no-injection simulations.

338 The background concentration of particles decays due to cloud scavenging. The decay rate
339 is dependent upon drop sizes and number concentration, and thus upon the background
340 concentration of aerosols. The total particle number concentration (N_T) in I200N/L200N
341 takes over 6 hours longer to reach below 10 cm^{-3} than in I50N/L50N. CCN injection results
342 in a steady accumulation of particles, reaching over 2000 cm^{-3} in some places directly along
343 the center of the injection plume. The increase in the in-cloud particle number generally
344 remains more confined to the center of the domain, spreading toward the edges more slowly.
345 The passive tracer is not scavenged by in-cloud processes, so it represents the maximum
346 possible area affected by CCN injection. Comparisons to the results of Wang et al. (2011)
347 reveal that the spreading of CCN throughout the domain is slower in the present study.

348 This model configuration is not equipped to provide calculations of supersaturation over
349 liquid water for accurate calculation of liquid water condensation/evaporation. As such,
350 the Wegener-Bergeron-Findelsen (WBF) process, whereby ice crystals grow at the expense
351 of liquid droplets in conditions where the air parcel is supersaturated with respect to ice
352 but subsaturated with respect to liquid water, is captured by the model, but the small
353 liquid sub-saturation is not explicitly represented. Although the impact of CCN injection
354 on droplet sizes does not directly affect droplet evaporation in the model, there is still
355 substantial impact on liquid water through interactions with ice nucleation and growth. In
356 the microphysical scheme used here, the initiation of ice nucleation by freezing droplets
357 depends on the availability of droplet number, and the freezing rate increases with drop size.
358 Both liquid water path and ice water path increase early in the simulations, with greater
359 increases for the more polluted background and the injection cases. In the injection cases,
360 liquid droplet number and ice crystal number also increase early in the simulations. This
361 likely indicates that existing ice particles are increasing in size, and new particles are being

362 nucleated. Injection causes a substantial decrease in liquid water particle size and a slight
 363 increase in ice particle size. The total ice water path (Figures 1d and 3d) and ice water
 364 content (Figure 8) are much smaller than those of liquid clouds, and the majority of ice
 365 water is represented as snow.

366 The results presented here are consistent with frequently observed Arctic cloud regimes
 367 that are CCN-limited. With weak aerosol sources, effective wet deposition of CCN, and
 368 aerosol-cloud-precipitation interactions, Arctic clouds can become depleted (Mauritsen *et al.*
 369 2011). These situations resemble our no-injection simulations, which are characterized by
 370 low CCN and low amounts of cloud cover. This suggests that the regions of boundary layer
 371 collapse shown in multiple figures are not necessarily uncommon in the Arctic.

372 3.2 Cloud Extent and Albedo Changes

373 The most salient question for MCB is whether our results indeed show cloud brightening,
 374 i.e., whether there are increases in cloud extent and cloud albedo due to particle injection.
 375 Because total liquid water is, to a large extent, controlled by ice nucleation processes, which
 376 differ between models, caution should be used when generalizing these results.

377 The model does not explicitly include calculations of cloud albedo, so we represent this
 378 quantity with a parameterization. The cloud top effective radius (r_e) can be approximated
 379 as

$$r_e \approx 1.08r_v \quad (4)$$

380 where r_v is the cloud drop mean volume radius (Rosenfeld *et al.* 2012). Liquid cloud optical
 381 depth (τ) is calculated as

$$\tau = \frac{3}{2\rho_w} \frac{\text{LWP}}{r_e} \quad (5)$$

382 where ρ_w is the density of liquid water, and LWP is the liquid water path (Stephens 1978).
 383 From this, liquid cloud albedo (α) can be calculated using the two-stream approximation
 384 (Bohren 1987):

$$\alpha = \frac{(1 - g)\tau}{2 + (1 - g)\tau} \quad (6)$$

385 where g is the (dimensionless) asymmetry parameter of the cloud droplets, assumed here to
 386 be 0.85.

387 Ice processes require a different formulation for calculating cloud albedo. Due to signifi-
 388 cant heterogeneity of ice crystal shapes, there is no standardized concept for an ice crystal
 389 effective radius (McFarquhar and Heymsfield, 1998). As a proxy, we use the volume mean
 390 radius of the ice crystals if taken as spherical particles:

$$r_v = \left[\frac{\text{IWP}}{N_i} \frac{3}{4\pi\rho_i} \right]^{1/3} \quad (7)$$

391 where IWP denotes the ice water path (ice crystals only), N_i is the number of ice crystal
 392 particles, and ρ_i is the density of ice, taken here to be 0.9 g cm^{-3} (Morrison and Grabowski,
 393 2008). Stephens *et al.* (1990) define the ice cloud droplet effective radius in terms of equiv-
 394 alent volume spheres, yielding a similar value to that of Equation 5. As such, our gross
 395 simplification is potentially reasonable for bulk parameterizations. Regardless, as we discuss
 396 below, ice optical depth is far lower than liquid optical depth, so the simplification used in
 397 Equation 7 should have negligible effects on our results. Given the vast uncertainty inherent
 398 in calculations of ice cloud albedo, we are unlikely to find a substantially better estimate
 399 of ice cloud albedo without detailed computations of the scattering phase functions of the
 400 implicitly assumed particle shapes (Mishchenko *et al.* 1996).

401 Taking the values calculated in Equation 7 as the ice crystal volume mean radius (r_v),

402 Ebert and Curry (1992) provide bulk calculations for ice cloud optical thickness (τ ; visible
403 wavelengths) and asymmetry parameter (g):

$$\tau = \text{IWP} \cdot (3.448 \times 10^{-3} + 2.431/r_v); \quad (8)$$

404

$$g = 0.7661 + 5.851 \times 10^{-4} \cdot r_v \quad (9)$$

405 where IWP has units of g m^{-2} and r_v has units of μm . Ice cloud albedo can then be calculated
406 using the two stream approximation, as in Equation 6.

407 Domain-averaged liquid cloud drop effective radius increases throughout the simulations
408 until the timing of the collapse of the boundary layer, at which point it sharply decreases
409 (Figure 1e). Similarly, ice crystal volume mean radius remains relatively constant until col-
410 lapse (Figure 1f). CCN injection results in a vastly reduced liquid cloud drop effective radius,
411 consistent with the first aerosol indirect effect, although liquid water content increases along
412 the injection track over the initial part of the simulation (Figures 1e and 8). As multiple
413 fields in Figures 1-4 show, the boundary layer collapse occurs in all no-injection simula-
414 tions, indicating that CCN injection as simulated here is sufficient to prevent this collapse.
415 Collapsed regions are characterized by small-scale convection that shows no evidence of or-
416 ganization (not shown); collapsed regions also arise in the injection simulations away from
417 the injection track. Because these simulations have no surface fluxes and no wind shear in
418 the initial meteorological profile, small-scale convection is likely driven primarily by radia-
419 tion, possibly in combination with latent heat exchange below the cloud base. This collapse
420 results in substantial decreases in liquid and ice water path, and the collapse is delayed by
421 approximately six hours in the polluted case as compared to the clean case. There are no
422 large differences in liquid cloud droplet effective radius between mixed-phase and liquid-only

423 phase simulations.

424 Cloud fraction shows substantial differences between liquid-only and mixed-phase simu-
425 lations (Figures 2g and 4g). In the liquid-only simulations, cloud fraction decreases substan-
426 tially ($> 40\%$) when the boundary layer collapses (also indicated by a substantial decrease
427 in cloud top; Figures 2b and 4b), and cloud fraction remains lower throughout the remainder
428 of the simulation. The timing of the decrease in cloud fraction is consistent with diurnal
429 variation. Conversely, in the mixed-phase simulations, the cloud fraction decreases when
430 the boundary layer collapses, but it then returns to cover nearly the entire domain. Liquid
431 cloud albedo also decreases in all simulations, coincident with the boundary layer collapse
432 (Figures 2e and 4e). Although domain-averaged ice cloud albedo decreases throughout the
433 simulations in the mixed-phase cases (Figures 2f and 4f), it increases in areas where the
434 liquid cloud albedo decreases (Figure 9). This suggests that inclusion of ice processes results
435 in a layer of optically thin ice clouds that has greater thickness in areas of less liquid cloud
436 cover. Liquid clouds are the dominant source of reflectivity (Figures 2, 4, and 9).

437 The substantial differences between the mixed phase simulations and the liquid-only sim-
438 ulations are likely due to the WBF process. Even slightly cooler temperatures in mixed-phase
439 clouds (as compared to liquid-only clouds) can sufficiently lower the minimum supersatur-
440 ation over ice required to form ice crystals, allowing the WBF process to occur. The
441 consequent creation of ice cloud lowers the liquid water path, reducing shortwave absorp-
442 tion. As such, we would expect the changes in cloud fraction to be consistent with diurnal
443 variations in shortwave radiation.

444 All simulations have initial increases in albedo due to CCN injection; the maximum
445 increase in domain albedo among all simulations is 0.23 (Figure 2e). Figure 9 shows an
446 initial increase in ice albedo along the CCN injection track, providing additional evidence

447 that CCN injection accelerates the WBF process.

448 CCN injection suppresses liquid precipitation (Figures 1c and 10), consistent with the
 449 second aerosol indirect effect. However, unlike the results of Wang *et al.* (2011), dynamical
 450 changes in circulation due to modification of precipitation are small, possibly in part because
 451 of the stability of the boundary layer. As such, we do not find regions of reduced albedo on
 452 the edges of the center track. The clouds along the injection track tend to persist and spread
 453 out over time, also consistent with the second indirect effect. In the mixed-phase simula-
 454 tions, although liquid precipitation is suppressed along the injection track, snow precipitation
 455 predominantly occurs along the track (Figure 10).

456 3.3 Cloud Susceptibility

457 Cloud albedo susceptibility can provide a useful indication of cloud modification in response
 458 to aerosols. Susceptibility of the cloud to brightening is given by

$$S = \frac{d \ln \alpha}{d \ln N_T} \quad (10)$$

459 where α is the cloud albedo, and N_T is the total number of potential CCN, taken here to be
 460 the sum of CDNC and interstitial CCN. Platnick and Twomey (1994) define susceptibility
 461 with the denominator only including CDNC and not interstitial CCN. We have opted for a
 462 modified definition in our study to include albedo increases for all *potential* CCN, not just
 463 active cloud droplets. One could analogously define the susceptibility of liquid water path
 464 to particle injection. We do not include such calculations here, as the low liquid water paths
 465 in our simulations make calculations of susceptibility very sensitive to variability.

466 Figure 11 shows a joint histogram of N_T and α , from which susceptibility can be inferred.

467 Comparison of the injection and no-injection simulations reveals two different regimes in each
468 simulation. The bow-shaped pattern that appears in all panels of Figure 11 are due to cloud
469 particles that are off the main injection track; the shape of this pattern is likely due to
470 the diurnal variation in liquid and ice water path (although conclusive attribution to this
471 mechanism is beyond our capabilities in the present study). The values corresponding to the
472 injection track are shown as a curve with lower frequency of occurrence that spans a larger
473 range of values of N_T . If only considering the values corresponding to the injection track, α
474 shows a positive increase with N_T , consistent with the first indirect effect that introducing
475 additional CCN will increase albedo. The concavity of these curves in Figure 11 is due to a
476 saturation effect: as additional CCN become CDNC, the relative amount of available water
477 for condensational growth of existing particles decreases, so changes in the size of the cloud
478 droplets are smaller.

479 As shown in the previous sections, the cloud layer in our simulations is, to some extent,
480 decoupled from the surface and is not heavily precipitating. This situation may not be appli-
481 cable to all meteorological conditions in the Arctic (e.g., M-PACE), and thus the calculations
482 of susceptibility presented here may differ for different situations (Klein *et al.* 2009).

483 **4 Discussion and Conclusions**

484 Our results show that injection of aerosols into the Arctic marine boundary layer, either
485 deliberately (geoengineering) or due to other mechanisms that would increase CCN in the
486 Arctic region, has the potential to brighten low clouds. Most of the albedo effects occur
487 in the liquid phase, the features of which are consistent with current knowledge of aerosol
488 indirect effects. In the simulations that include ice processes, some of the liquid water is con-
489 verted to ice, resulting in low in-cloud ice water content. Injection of CCN into mixed-phase

490 clouds results in smaller liquid water increases than in the liquid-only simulations through
491 interactions with ice nucleation and growth. The boundary layer collapse is coincident with
492 substantial precipitation of water (Figure 10), both in liquid and ice form. The precipita-
493 tion may indeed contribute toward the boundary layer collapse through reductions in CCN
494 and liquid water path. Injection of CCN into a relatively unpolluted environment results in
495 greater albedo increases than injection into polluted environments, consistent with current
496 knowledge about aerosol-cloud interactions.

497 The mechanisms governing the albedo and lifetime increases of the clouds in our sim-
498 ulations are straightforward. Evidence for the first and second aerosol indirect effects is
499 clearly visible, with few complicating factors, unlike the results of Wang *et al.* (2011) for
500 warm clouds, in which precipitation induced strong dynamical circulation changes in cloud
501 cover. The lack of strong circulation changes in our study is likely due to a combination of
502 low temperatures and low precipitation, resulting in small latent heating and cooling, and
503 thus limiting mesoscale dynamical changes. The effects of including surface sensible and
504 latent heat fluxes on dynamical circulation changes will be addressed in future work; these
505 choices could partially explain both the initial decoupling of the cloud layer from the sub-
506 cloud layer and the substantially lower liquid and ice water paths than in M-PACE, which
507 was a more well-mixed case (Klein *et al.* 2009). Altering the surface fluxes could in turn
508 change the susceptibility of the clouds to changes in aerosol concentration. Insofar as the
509 microphysical schemes used in our simulations accurately represent the processes involved
510 in MCB, the microphysical effects of Arctic CCN injection appear to be more predictable
511 than those of MCB in warm clouds, although some of this predictability is likely due to our
512 simplified experimental design (no initial wind shear, no surface fluxes, and a particular ice
513 nucleation parameterization). Our results show this holds for both liquid-only and mixed-

514 phase cold clouds. As stated in Section 3.2, the results presented here are likely dependent
515 upon the microphysical scheme used and may not be broadly generalizable (e.g., Morrison
516 *et al.*, 2011). As of yet, the effects of the initial meteorological profile on our results are
517 unclear, particularly the effects of the strong inversion present in our setup. Potential future
518 work could include initial profiles that correspond to measurements taken during other field
519 campaigns, such as M-PACE or SHEBA. Moreover, a horizontal grid spacing of 300 m may
520 not fully resolve large eddies in a boundary layer that is 1.5 km deep; further investigations
521 could explore the effects of horizontal resolution on our results.

522 Entrainment processes at the top of marine low clouds occur in very thin layers (Stevens
523 *et al.*, 2005). Our chosen vertical resolution of ~ 30 m is too coarse to accurately capture these
524 features. We performed additional simulations with a vertical resolution of ~ 10 m but did
525 not find any substantive changes in our results (not pictured). The results of Stevens *et al.*
526 (2005) suggest that to properly resolve entrainment issues would require vertical resolution
527 that is an order of magnitude finer than in our simulations, accompanied by commensurately
528 fine horizontal resolution to properly resolve eddy structure. The required computational
529 power to conduct the present simulations with such fine resolution is beyond our means.
530 The coarse vertical resolution of our simulations could result in underrepresentation of many
531 different processes, each of which either enhances or diminishes entrainment. As such, we are
532 unable to make conclusions about the effects of vertical resolution on our results. Regardless,
533 we believe the effect of entrainment on mixing was reasonably captured in our simulations,
534 based on previous studies of subtropical marine boundary layer clouds with a similar model
535 configuration (Wang *et al.*, 2011).

536 To put our results into context, we can do a simple back-of-the-envelope calculation of
537 the effects of Arctic MCB on the global radiation budget, assuming that the results in our

538 domain can be extrapolated to all open ocean regions of the Arctic. We focus only on open
539 ocean areas, as sea ice and snow-covered land already have higher albedos than marine low
540 clouds, so brighter clouds over these regions will have minimal impacts on the radiation
541 budget. As an illustration, we determined open ocean fraction in the Arctic (66.56°N to
542 90°N) as calculated from monthly mean sea ice extent data for 2012 (Meier *et al.*, 2013;
543 Peng *et al.*, 2013). Taking the maximum domain albedo increase from our results of 0.23,
544 the additional radiative forcing from Arctic geoengineering would be an average of -0.45 W
545 m^{-2} globally, or -10.94 W m^{-2} over the Arctic. At most, the radiative impacts would have a
546 small (although potentially non-negligible) effect on the global radiation budget, suggesting
547 Arctic MCB could not serve as the sole means of offsetting the net radiative forcing from
548 greenhouse gas emissions. However, the local effects on the Arctic radiation budget could
549 be quite substantial, even if the actual effect is an order of magnitude smaller than the
550 maximum effect as calculated from our results. These results may also be diminished if
551 cooling causes sea ice growth, reducing the area of open ocean. Moreover, longwave forcing
552 from Arctic clouds has a positive correlation with liquid water path, which is enhanced by
553 CCN injection (Shupe and Intrieri, 2004). This increase in longwave forcing could offset
554 some of the shortwave forcing from brightening, although the increase in longwave surface
555 cloud forcing saturates at liquid water path values of approximately 60 g m^{-2} , so determining
556 the net impact of this longwave effect is not straightforward. The increase in downwelling
557 longwave radiation could also increase latent heating and hence moisture flux from the surface
558 into the clouds, forming a feedback loop (Garrett and Zhao, 2006; Lubin and Vogelmann,
559 2006; Morrison *et al.* 2012). For low liquid water paths ($<30\text{-}50 \text{ g m}^{-2}$), there is also a droplet
560 size effect on longwave cloud forcing (Garrett and Zhao, 2006; Lubin and Vogelmann, 2006).

561 The simulations presented here involve injection of CCN with aerosol properties, including

562 hygroscopicity and thermodynamics related to cloud particle activation, corresponding to
563 ammonium sulfate. Explicitly representing a different type of aerosol (the most commonly
564 studied aerosol for MCB is sea salt) could modify the effectiveness of MCB. Partanen *et*
565 *al.* (2012) and Alterskjær *et al.* (2013) showed the aerosol direct effect of sea salt aerosols
566 could be a substantial portion of the total radiative impact of MCB. Jenkins and Forster
567 (2013) explicitly modeled the effects of creating CCN via evaporating sea water droplets;
568 including these mechanisms can lessen albedo increases, in some cases nearly negating the
569 aerosol indirect effects. Moreover, the size of the sea salt aerosols can affect the results due
570 to a competition effect between the injected sea salt and other particles. Further studies
571 could incorporate all of these effects by explicitly simulating microphysics specific to sea
572 salt aerosols and how they differ as compared to sulfate aerosols. Alternatively, simulating
573 different aerosols that serve as effective ice nuclei could result in more water being retained
574 as ice, enhancing ice cloud albedo.

575 Cloud ice crystal size is assumed to have a fixed size distribution width, although the
576 modal radius is allowed to vary. Ovchinnikov *et al.* (2014) found that ice water path,
577 and hence calculations of cloud albedo (Equation 6), is strongly dependent upon accurate
578 representations of the ice crystal size distribution. According to the results of Ovchinnikov
579 *et al.*, our calculations of ice water path may have been underestimated, implying our results
580 for ice albedo could be more dramatic. Replications of our study with different microphysical
581 schemes could be useful in verifying our results.

582 The clean cases have a collapsed boundary layer away from the injection track, consistent
583 with features described by Ackerman *et al.* (1993) and Wang *et al.* (2010). No simulation
584 shows indications of organized convection or cellular structure. This is possibly in part due
585 to holding heat and moisture surface fluxes at zero (Kazil *et al.* 2014); a future study is

586 planned that will investigate the effects of these fluxes on the results presented here. The
587 boundary layer collapse could also be due to the choice of not including a background aerosol
588 source, as discussed in Section 2.3. Although having no aerosol source in the model domain
589 is unrealistic for a 30 hour period, our simulations include the process of gradual aerosol
590 removal. As such, our simulations show the impact of aerosol injection into a wide variety
591 of different aerosol and cloud background conditions. Another potential exploration for the
592 lack of cellular structure is reduced evaporative cooling below the cloud base due to the small
593 liquid water content as compared to warm clouds. In the current setup, when cloud particles
594 evaporate and resuspend the aerosols, the aerosols return to their original size, whereas they
595 should grow in size due to collision/coalescence. Thus the resuspended aerosols are too small,
596 making them less effective CCN than they would otherwise be if aerosol mass were conserved.
597 Conserving aerosol mass, such as in the scheme of Lebo and Morrison (2013) could delay
598 the collapse of the boundary layer, although further simulations would be needed to test
599 this. A further reason for the boundary layer collapse could be the choice of no initial wind
600 shear. In the presence of stronger shear throughout the simulation, the injected CCN would
601 be distributed more evenly across the domain, which could prevent boundary layer collapse
602 in regions away from the injection track and help to maintain the cloud through increased
603 turbulence. Inclusion of initial shear may also reduce the oscillatory patterns in Figures 1-2,
604 as the redistribution of the CCN by wind would mean that additional injection would not
605 be into such CCN-rich areas.

606 Some of the results show a dependence upon the diurnal cycle, although we are unable
607 to make firm conclusions about the effects of diurnal variation from our study. We only
608 simulated one full diurnal cycle, so it is unclear whether the features we show have some
609 component of diurnal variation that is masked by the transient nature of the simulations.

610 Moreover, we used a particular shortwave radiation scheme; different radiation schemes may
611 have different impacts on the results. Isolating the effects of the boundary layer collapse, as
612 well as inclusion of surface sensible and latent heat fluxes, could give a better indication of
613 the timing of shortwave impacts on our results.

614 Our results only represent process-level studies. Determining the actual effects of CCN
615 injection into the Arctic marine boundary layer, either inadvertently or advertently, would
616 require a great deal of further work. Moreover, there are many concerns with geoengineering
617 that are not represented here, all of which would be assessed by appropriate governance
618 structures before a decision to deploy geoengineering is made. Nevertheless, process-modeling
619 studies like ours can be useful in determining some of the behaviors and underlying physical
620 mechanisms behind natural and anthropogenic emissions of CCN into Arctic marine low
621 clouds.

622 **Acknowledgments**

623 We thank Mikhail Ovchinnikov for helpful discussions about our simulations and three anony-
624 mous reviewers for their constructive comments. This research was supported by the Office
625 of Science of the U.S. Department of Energy (DOE) Earth System Modeling program. BK
626 acknowledges support from the Fund for Innovative Climate and Energy Research (FICER).
627 The Pacific Northwest National Laboratory is operated for the U.S. Department of Energy
628 by Battelle Memorial Institute under contract DE-AC05-76RLO 1830.

References

- 629
- 630 1. Abdul-Razzak, H. and Ghan, S. J. 2000 A parameterization of aerosol activation: 2.
631 Multiple aerosol types. *J. Geophys. Res.* **105**, 6837-6844. (doi:10.1029/1999JD901161)
 - 632 2. Ackerman, A. S., Toon, O. B., and Hobbs, P. V. 1993 Dissipation of marine strati-
633 form clouds and collapse of the marine boundary layer due to the depletion of cloud
634 condensation nuclei by clouds. *Science* **262**, 226-229.
 - 635 3. Ackerman, A. S., Toon, O. B., Stevens, D. E. and Coakley Jr, J. A. 2003 Enhancement
636 of cloud cover and suppression of nocturnal drizzle in stratocumulus polluted by haze.
637 *Geophys. Res. Lett.* **30**, 1381. (doi:10.1029/2002GL016634)
 - 638 4. Albrecht, B. A. 1989 Aerosols, cloud microphysics, and fractional cloudiness. *Science*
639 **245**, 1227-1230.
 - 640 5. Alterskjær, K., *et al.* 2013 Sea-salt injections into the low-latitude marine boundary
641 layer: The transient response in three Earth system models. *J. Geophys. Res.* **118**,
642 12195-12206. (doi:10.1002/2013JD020432)
 - 643 6. Bigg, E. K. 1953 The formation of atmospheric ice crystals by the freezing of droplets.
644 *Q. J. Roy. Meteor. Soc.* **79**, 510-519. (doi:10.1002/qj.49707934207)
 - 645 7. Birch, C. E., Brooks, I. M., Tjernström, M., Milton, S. F., Earnshaw, P., Söderberg,
646 S., and Persson P. O. G. 2009 The performance of a global and mesoscale model
647 over the central Arctic Ocean during late summer. *J. Geophys. Res.* **114**, D13104.
648 (doi:10.1029/2008JD010790)

- 649 8. Bohren, C. F. 1987 Multiple scattering of light and some of its observable consequences.
650 *Amer. J. Phys.* **55**, 524-533.
- 651 9. Boucher, O. *et al.* 2013 Clouds and Aerosols. In: *Climate Change 2013: The Physical*
652 *Science Basis. Contribution of Working Group I to the Fifth Assessment Report of the*
653 *Intergovernmental Panel on Climate Change* [Stocker, T.F., D. Qin, G.-K. Plattner,
654 M. Tignor, S.K. Allen, J. Boschung, A. Nauels, Y. Xia, V. Bex and P.M. Midgley
655 (eds.)]. Cambridge University Press, Cambridge, United Kingdom and New York, NY,
656 USA.
- 657 10. Coakley Jr., J. A. *et al.* 2000 The appearance and disappearance of ship tracks on
658 large spatial scales. *J. Atmos. Sci.* **57**, 2765-2778.
- 659 11. Chen, Y.-C., Christensen, M. W., Xue, L., Sorooshian, A., Stephens, G. L., Rasmussen,
660 R. M., and Seinfeld, J. H. 2012 Occurrence of lower cloud albedo in ship tracks. *Atmos.*
661 *Chem. Phys.* **12**, 8223-8235. (doi:10.5194/acp-12-8223-2012)
- 662 12. Collins, W. D., *et al.* 2006 The formulation and atmospheric simulation of the Com-
663 munity Atmosphere Model Version 3 (CAM3). *J. Climate* **19**, 2144-2161.
- 664 13. Curry, J. A. *et al.* 2000 FIRE Arctic Clouds Experiment. *Bull. Amer. Meteor. Soc.*
665 **81**, 5-29.
- 666 14. Deardorff, J. W. 1972 Numerical investigation of neutral and unstable planetary bound-
667 ary layers. *J. Atmos. Sci.* **29**, 91-115.
- 668 15. Ebert, E. E. & Curry, J. A. 1992 A parameterization of ice cloud optical properties for
669 climate models. *J. Geophys. Res.* **97**, 3831-3836. (doi:10.1029/91JD02472)

- 670 16. Feingold, G., Kreidenweis, S. M., Stevens, B., and Cotton, W. R. 1996 Numerical
671 simulations of stratocumulus processing of cloud condensation nuclei through collision-
672 coalescence. *J. Geophys. Res.* **101**, 21391-21402. (doi:10.1029/96JD01552)
- 673 17. Fridlind, A. M. *et al.* 2012 A FIRE-ACE/SHEBA case study of mixed-phase Arctic
674 boundary layer clouds: Entrainment rate limitations on rapid primary ice nucleation
675 processes. *J. Atmos. Sci.* **69**, 365-389. (doi:10.1175/JAS-D-11-052.1)
- 676 18. Garrett, T. and Zhao, C. Increased Arctic cloud longwave emissivity associated with
677 pollution from mid-latitudes. *Nature* **440**, 787-789.
- 678 19. Jenkins, A. K. L. & Forster, P. M. 2013 The inclusion of water with the injected aerosol
679 reduces the simulated effectiveness of marine cloud brightening. *Atm. Sci. Lett.* **14**,
680 164-169. (doi: 10.1002/asl2.434)
- 681 20. Jenkins, A. K. L., Forster, P. M., & Jackson, L. S. 2013 The effects of timing and rate of
682 marine cloud brightening aerosol injection on albedo changes during the diurnal cycle of
683 marine stratocumulus clouds. *Atmos. Chem. Phys.* **13**, 1659-1673. (doi:10.5194/acp-
684 13-1659-2013)
- 685 21. Kazil, J., Feingold, G., Wang, H., and Yamaguchi, T. 2014 On the interaction between
686 marine boundary layer cellular cloudiness and surface heat fluxes. *Atm. Chem. Phys.*
687 **14**, 61-79. (doi:10.5194/acp-14-61-2014)
- 688 22. Klein, S. A. *et al.* 2009 Intercomparison of model simulations of mixed-phase clouds
689 observed during the ARM Mixed-Phase Arctic Cloud Experiment. I: Single-layer cloud.
690 *Q. J. Roy. Meteor. Soc.* **135**, 979-1002. (doi:10.1002/qj.416)

- 691 23. Korhonen, H., Carslaw, K. S., & Romakkaniemi, S. 2010 Enhancement of marine
692 cloud albedo via controlled sea spray injections: A global model study of the influence
693 of emission rates, microphysics and transport. *Atmos. Chem. Phys.* **10**, 4133-4143.
694 (doi:10.5194/acp-10-4133-2010)
- 695 24. Kravitz, B. *et al.* 2013 Sea spray geoengineering experiments in the Geoengineer-
696 ing Model Intercomparison Project (GeoMIP): Experimental design and preliminary
697 results. *J. Geophys. Res.* **118**, 11175-11186. (doi:10.1002/jgrd.50856)
- 698 25. Latham, J. 1990 Control of global warming? *Nature* **347**, 339-340.
- 699 26. Latham, J. 2002 Amelioration of global warming by controlled enhancement of the
700 albedo and longevity of low-level maritime clouds. *Atmos. Sci. Lett.* **3**, 52-58.
701 (doi:10.1006/asle.2002.0099)
- 702 27. Latham, J. *et al.* 2008 Global temperature stabilization via controlled albedo enhance-
703 ment of low-level maritime clouds. *Phil. Trans. Roy. Soci. A* **366**, 3969-3987.
- 704 28. Lebo, Z. J. and Morrison, H. 2013 A novel scheme for parameterizing aerosol processing
705 in warm clouds. *J. Atmos. Sci.* **70**, 3576-3598. (doi:10.1175/JAS-D-13-045.1)
- 706 29. Lubin, D. and Vogelmann, A. 2006 A climatologically significant aerosol long-wave
707 indirect effect in the Arctic. *Nature* **439**, 453-456.
- 708 30. Mauritsen, T. *et al.* 2011 An Arctic CCN-limited cloud-aerosol regime. *Atmos. Chem.*
709 *Phys.* **11**, 165-173. (doi:10.5194/acp-11-165-2011)
- 710 31. McFarquhar, G. M. & Heymsfield, A. J. 1998 The definition and significance of an
711 effective radius for ice clouds. *J. Atmos. Sci.* **55**, 2039-2052.

- 712 32. McFarquhar, G. M. *et al.* 2011, Indirect and Semi-Direct Aerosol Campaign: the
713 impact of Arctic aerosols on clouds. *Bull. Amer. Meteor. Soc.* **92**, 183-201.
- 714 33. Meier, W., Fetterer, F., Savoie, M., Mallory, S., Duerr, R., & Stroeve, J. 2013 NOAA/NSIDC
715 Climate Data Record of Passive Microwave Sea Ice Concentration. Version 2. Boulder,
716 Colorado USA: National Snow and Ice Data Center. (doi:10.7265/N55M63M1)
- 717 34. Mischchenko, M. I., Rossow, W. B., Macke, A., & Lacis, A. A. 1996 Sensitivity of
718 cirrus cloud albedo, bidirectional reflectance and optical thickness retrieval accuracy
719 to ice particle shape. *J. Geophys. Res.* **101**, 16973-16985.
- 720 35. Mitra, S. K., Brinkmann, J., and Pruppacher, H. R. 1992 A wind tunnel study on
721 the drop-to-particle conversion. *J. Aerosol Sci.* **23**, 245-256. (doi:10.1016/0021-
722 8502(92)90326-Q)
- 723 36. Morrison, H., Curry, J. A., and Khvorostyanov, V. I. 2005 A new double-moment
724 microphysics parameterization for application in cloud and climate models. Part I:
725 Description. *J. Atmos. Sci.* **62**, 1665-1677.
- 726 37. Morrison, H. and Pinto, J. O. 2005 Mesoscale modeling of springtime Arctic mixed-
727 phase stratiform clouds using a new two-moment bulk microphysics scheme. *J. Atmos.*
728 *Sci.* **62**, 3683-3704. (doi:10.1175/JAS3564.1)
- 729 38. Morrison, H. & Grabowski, W. W. 2008 A novel approach for representing ice micro-
730 physics in models: Descriptions and tests using a kinematic framework. *J. Atmos. Sci.*
731 **65**, 1528-1548.
- 732 39. Morrison, H., Thompson, G., and Tatarskii, V. 2009 Impact of cloud microphysics
733 on the development of trailing stratiform precipitation in a simulated squall line:

- 734 Comparison of one-and two-moment schemes. *Mon. Wea. Rev.* **137**, 991-1007.
735 (doi:10.1175/2008MWR2556.1)
- 736 40. Morrison, H. *et al.* 2011, Intercomparison of cloud model simulations of Arctic mixed-
737 phase boundary layer clouds observed during SHEBA. *J. Adv. Model. Earth Syst.* **3**,
738 M06003. (doi:10.1029/2011MS000066)
- 739 41. Morrison, H., de Boer, G., Feingold, G., Harrington, J., Shupe, M. D., and Sulia,
740 K. 2012 Resilience of persistent Arctic mixed-phase clouds. *Nature Geosc.* **5**, 11-17.
741 (doi:10.1038/ngeo1332)
- 742 42. Ovchinnikov, M. *et al.* 2014 Intercomparison of large-eddy simulations of Arctic mixed-
743 phase clouds: Importance of ice size distribution assumptions. *J. Adv. Modeling Earth*
744 *Sys.* in press. (doi:10.1002/2013MS000282)
- 745 43. Partanen, A.-I. *et al.* 2012 Direct and indirect effects of sea spray geoengineering and
746 the role of injected particle size. *J. Geophys. Res.* **117**, D02203. (doi:10.1029/2011JD016428)
- 747 44. Peng, G., Meier, W., Scott, D., & Savoie, M. 2013 A long-term and reproducible passive
748 microwave sea ice concentration data record for climate studies and monitoring. *Earth*
749 *Syst. Sci. Data* **5**, 311-318. (doi:10.5194/essd-5-311-2013)
- 750 45. Platnick, S. & Twomey, S. 1994 Determining the susceptibility of cloud albedo to
751 changes in droplet concentration with the Advanced Very High Resolution Radiometer.
752 *J. Appl. Meteor.* **33**, 334-347.
- 753 46. Pringle, K. J., Carslaw, K. S., Fan, T., Mann, G. W., Hill, A., Stier, P., Zhang, K., &
754 Tost, H. 2012 A multi-model assessment of the impact of sea spray geoengineering on

- 755 cloud droplet number. *Atmos. Chem. Phys.* **12**, 11647-11663. (doi:10.5194/acp-12-
756 11647-2012)
- 757 47. Radke, L. F., Coakley Jr., J. A., and King, M. D. 1989 Direct and remote sensing
758 observations of the effects of ships on clouds. *Science* **246**, 1146-1149.
- 759 48. Randall, D. A., Coakley Jr., J. A., Fairall, C. W., Kropfli, R. A., and Lenschow, D.
760 H. 1984 Outlook for research on subtropical marine stratiform clouds. *Bull. Amer.*
761 *Meteor. Soc.* **65**, 1290-1301.
- 762 49. Rasch, P. J., Latham, J., and Chen, C.-C. 2009 Geoengineering by cloud seeding: Influ-
763 ence on sea ice and climate system. *Environ. Res. Lett.* **4**, 045112. (doi:10.1088/1748-
764 9326/4/4/045112)
- 765 50. Rosenfeld, D., Wang, H., and Rasch, P. J. 2012 The roles of cloud drop effective radius
766 and LWP in determining rain properties in marine stratocumulus. *Geophys. Res. Lett.*
767 **39**, L13801. (doi:10.1029/2012GL052028)
- 768 51. Salter, S., Sortino, G., and Latham, J. 2008 Sea-going hardware for the cloud albedo
769 method of reversing global warming. *Phil. Trans. Roy. Soc. A* **366**, 3989-4006.
- 770 52. Shupe, M. D. and Intrieri J. M. 2004 Cloud radiative forcing of the Arctic surface: The
771 influence of cloud properties, surface albedo, and solar zenith angle. *J. Climate* **17**,
772 616-628.
- 773 53. Skamarock, W. C., *et al.* 2008 A Description of the Advanced Research WRF Version
774 3. Tech. Rep. NCAR/TN-475+STR, National Center for Atmospheric Research,
775 Boulder, CO, USA.

- 776 54. Stephens, G. L. 1978 Radiation profiles in extended water clouds. II: Parameterization
777 schemes. *J. Atmos. Sci.* **35**, 2123-2132. (doi:10.1175/1520-0469(1978)035<2123:RPIEWC>2.0.CO;2)
- 778 55. Stephens, G. L., Tsay, S.-C., Stackhouse, P. W., and Flatau, P. J. 1990 The relevance
779 of the microphysical and radiative properties of cirrus clouds to climate and climatic
780 feedback. *J. Atmos. Sci.* **47**, 1742-1754.
- 781 56. Stevens, B. *et al.* 2005 Evaluation of large-eddy simulations via observations of noctur-
782 nal marine stratocumulus. *Mon. Wea. Rev.* **133**, 1443-1462. (doi:10.1175/MWF2930.1)
- 783 57. Stuart, G. S. *et al.* 2013 Reduced efficacy of marine cloud brightening geoengineering
784 due to in-plume aerosol coagulation: Parameterization and global implications. *Atmos.*
785 *Chem. Phys.* **13**, 10385-10396. (doi:10.5194/acp-13-10385-2013)
- 786 58. Twomey, S. 1977 Influence of pollution on shortwave albedo of clouds. *J. Atmos. Sci.*
787 **34**, 1149-1152.
- 788 59. Verlinde, J. *et al.* 2007 The Mixed-Phase Arctic Cloud Experiment (M-PACE). *Bull.*
789 *Amer. Meteor. Soc.* **88**, 205-221.
- 790 60. Wang, H. and Feingold, G. 2009 Modeling mesoscale cellular structures and drizzle in
791 marine stratocumulus. Part II: The microphysics and dynamics of the boundary region
792 between open and closed cells. *J. Atmos. Sci.* **66**, 3257-3275.
- 793 61. Wang, H., Skamarock, W. C., and Feingold, G. 2009 Evaluation of scalar advection
794 schemes in the Advanced Research WRF model using large-eddy simulations of aerosol-
795 cloud interactions. *Mon. Weather Rev.* **137**, 2547-2558. (doi:10.1175/2009MWR2820.1)

- 796 62. Wang, H., Feingold, G., Wood, R., and Kazil, J. 2010 Modelling microphysical and me-
797 teorological controls on precipitation and cloud cellular structures in Southeast Pacific
798 stratocumulus. *Atmos. Chem. Phys.* **10**, 6347-6362. (doi:10.5194/acp-10-6347-2010)
- 799 63. Wang, H., Rasch, P. J., & Feingold, G. 2011 Manipulating marine stratocumulus cloud
800 amount and albedo: A process-modeling study of aerosol-cloud-precipitation interac-
801 tions in response to injection of cloud condensation nuclei. *Atmos. Chem. Phys.* **11**,
802 4237-4249. (doi:10.5194/acp-11-4237-2011)
- 803 64. Warren, S. G., Hahn, C. J., London, J., Chervin, R. M., and Jenne, R. L. 1998 Global
804 distribution of total cloud and cloud type amounts over the ocean. NCAR Tech. Note
805 TN-317 + STR/DOE Tech. Rep. ER-0406.
- 806 65. Wood, R. 2012 Stratocumulus clouds. *Mon. Wea. Rev.* **140** 2373-2423. (doi:10.1175/MWR-
807 D-11-00121.1)

Table 1: The initial meteorological profile used in all simulations. θ denotes potential temperature (K), q is the total water mixing ratio (g kg^{-1}), u and v are horizontal wind speeds in the x and y directions, respectively (m s^{-1}), and z denotes altitude (m).

Altitude (m)	θ (K)	q (g kg^{-1})	u (m s^{-1})	v (m s^{-1})
0-400	$265 + 0.004(z - 400)$	$1.5 - 0.00075(z - 400)$	0	0
400-825	265	1.5	0	0
825-1500	$266 + (z - 825)^{0.3}$	1.2	0	0

Table 2: Naming conventions and descriptions of the eight simulations used in this study. “I” indicates inclusion of ice processes, and “L” indicates liquid only. “N” indicates no CCN injection, and “G” indicates CCN injection (geoengineering). Further descriptions of the sensitivity studies performed here are given in Section 2.

Name	Background CCN (cm^{-3})	Ice processes included	CCN Injection (geoengineering)
I50N	50	yes	no
I50G	50	yes	yes
I200N	200	yes	no
I200G	200	yes	yes
L50N	50	no	no
L50G	50	no	yes
L200N	200	no	no
L200G	200	no	yes

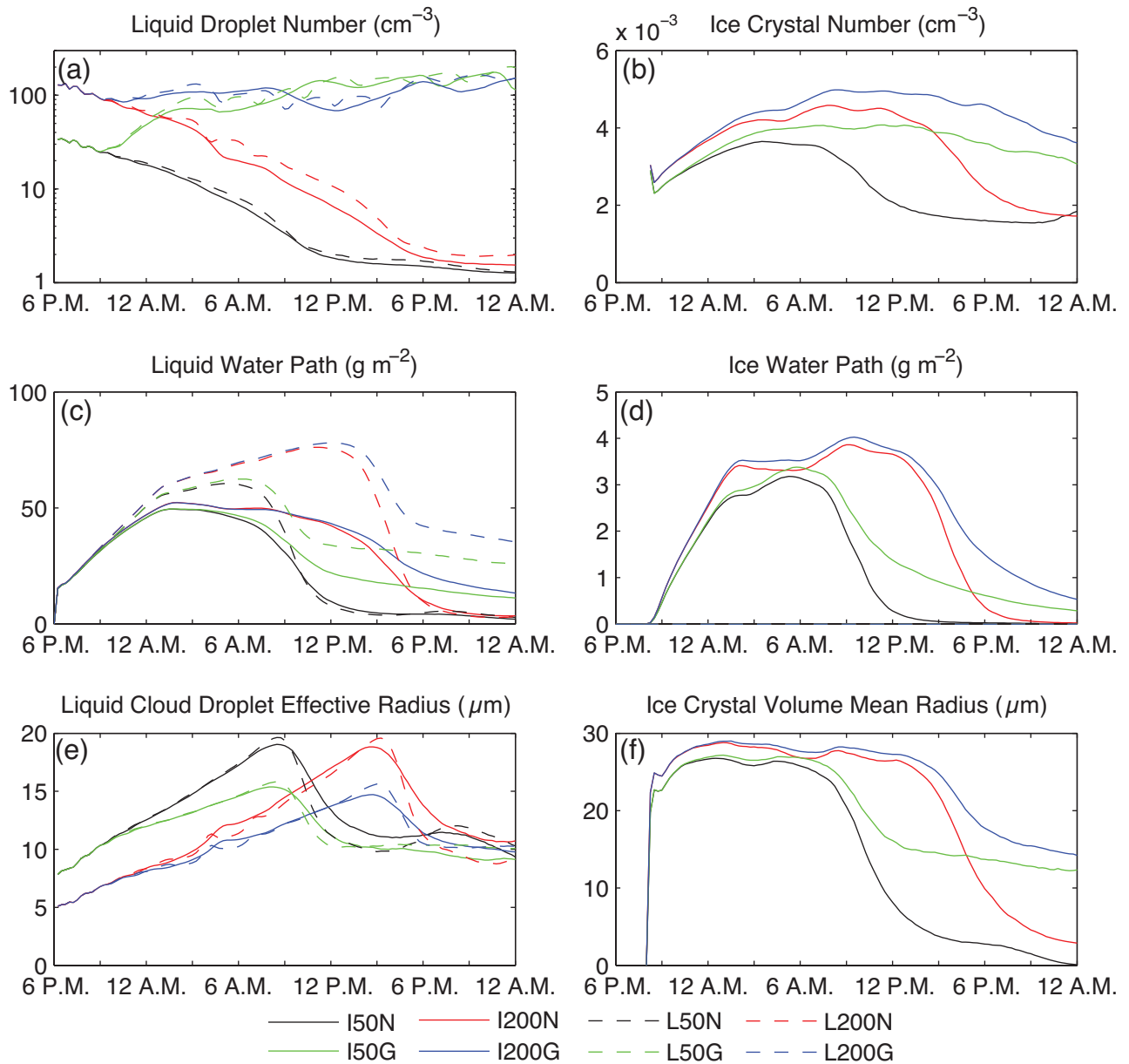


Figure 1: Domain-averaged time series of a) liquid droplet number; b) ice crystal number; c) liquid water path; d) ice water path (includes ice crystal, snow, and graupel); e) liquid cloud droplet effective radius (Equation 4); and f) ice crystal volume mean radius (Equation 7). Values in panels a, c, and e are averaged over all grid boxes containing liquid cloud. Panels b, d, and f are averaged over grid boxes containing ice. Experiments are listed in Table 2.

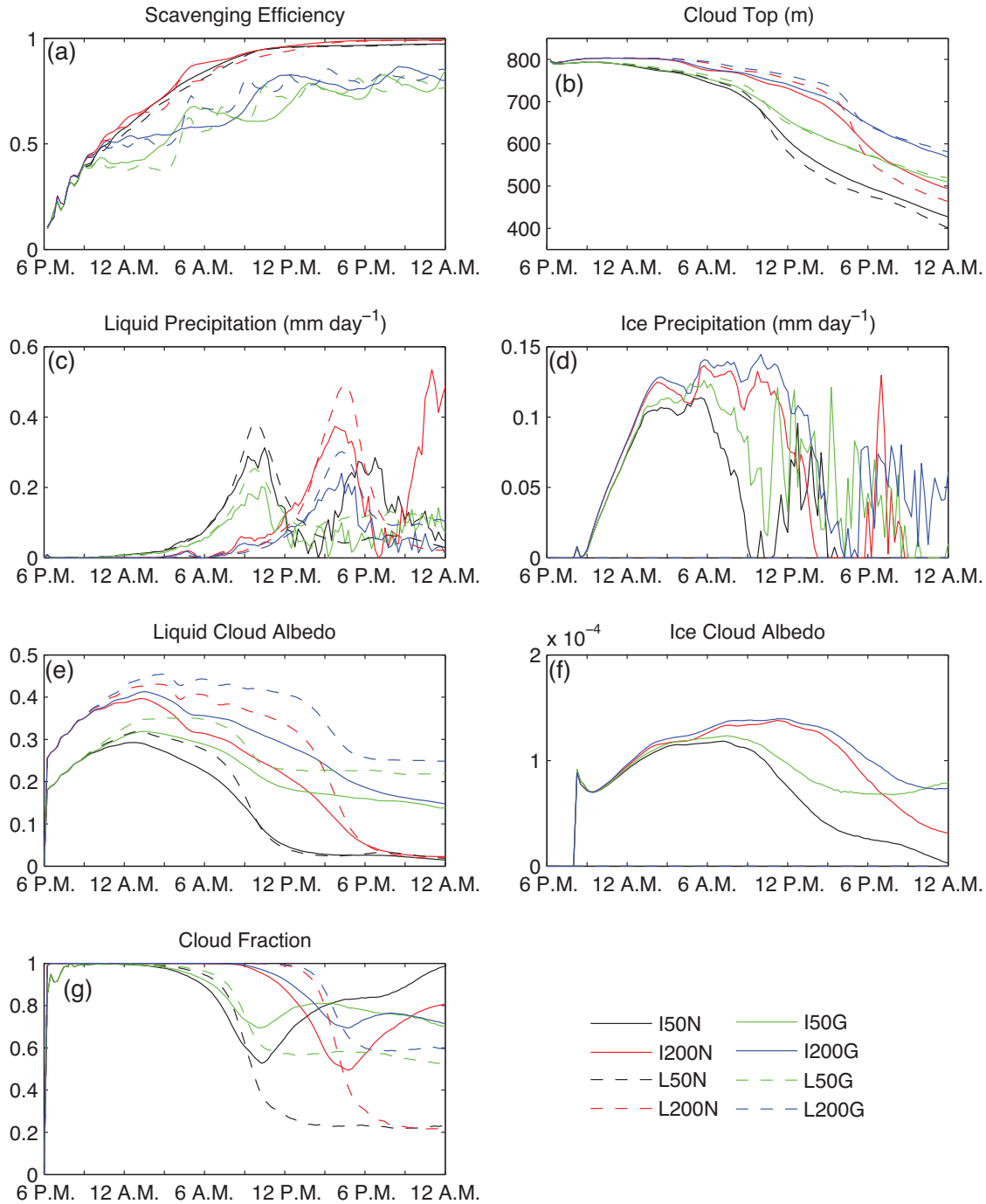


Figure 2: Domain-averaged time series of a) scavenging efficiency (Equation 3); b) cloud top; c) liquid precipitation; d) ice precipitation; e) liquid cloud albedo (Equation 6); f) ice cloud albedo (Equations 5, 6, 7); and g) cloud fraction. Panels e and f are averaged over the entire domain; grid boxes with no cloud are given an albedo of 0. Panel g is calculated by dividing the total number of columns with cloud by the total number of columns in the domain. Criteria for determining cloudy grid cells are given at the end of Section 2.3. Experiments are listed in Table 2.

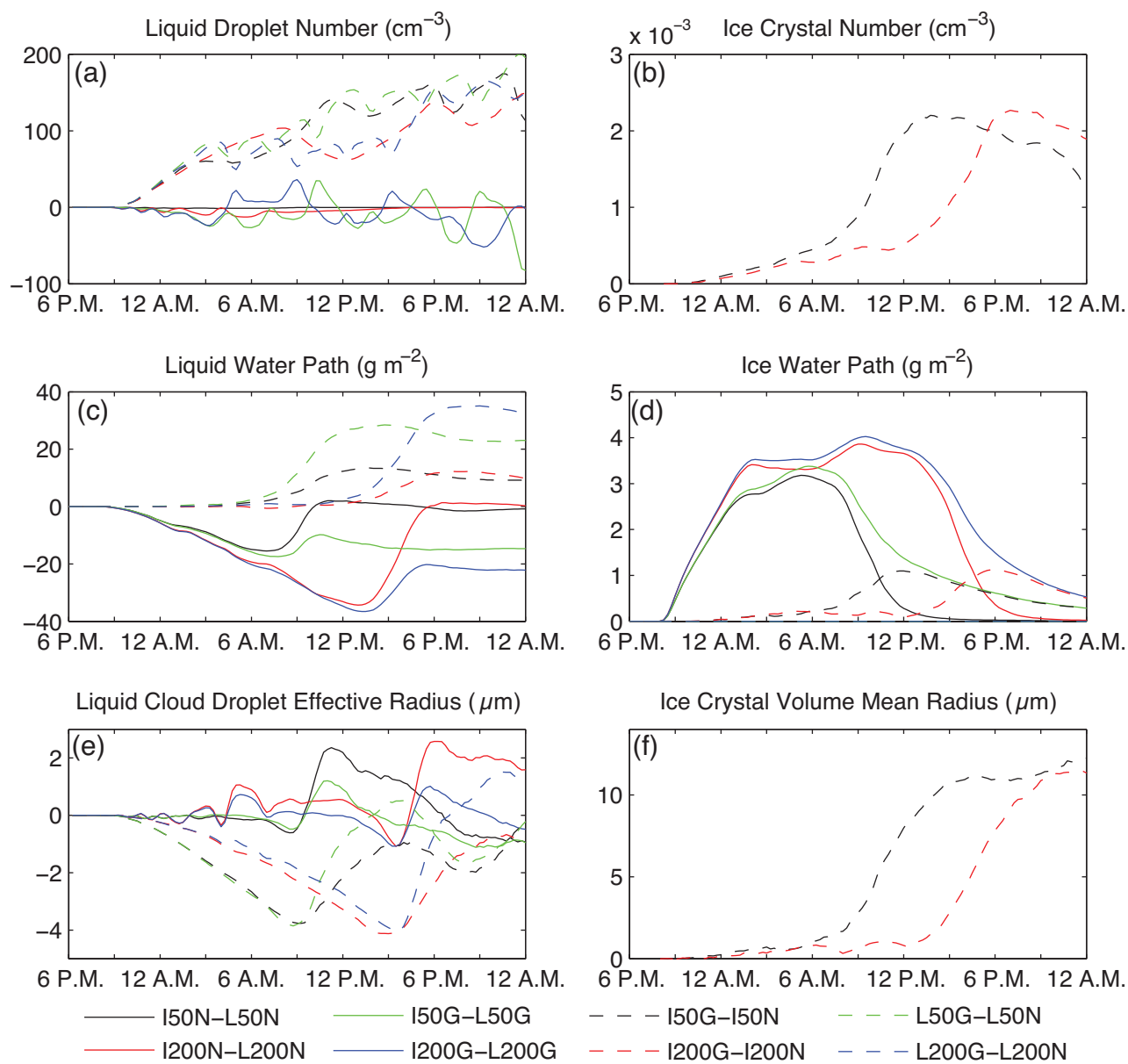


Figure 3: Same as Figure 1 but showing differences between injection vs no injection (dashed lines) and inclusion of ice processes vs exclusion of ice processes (solid lines).

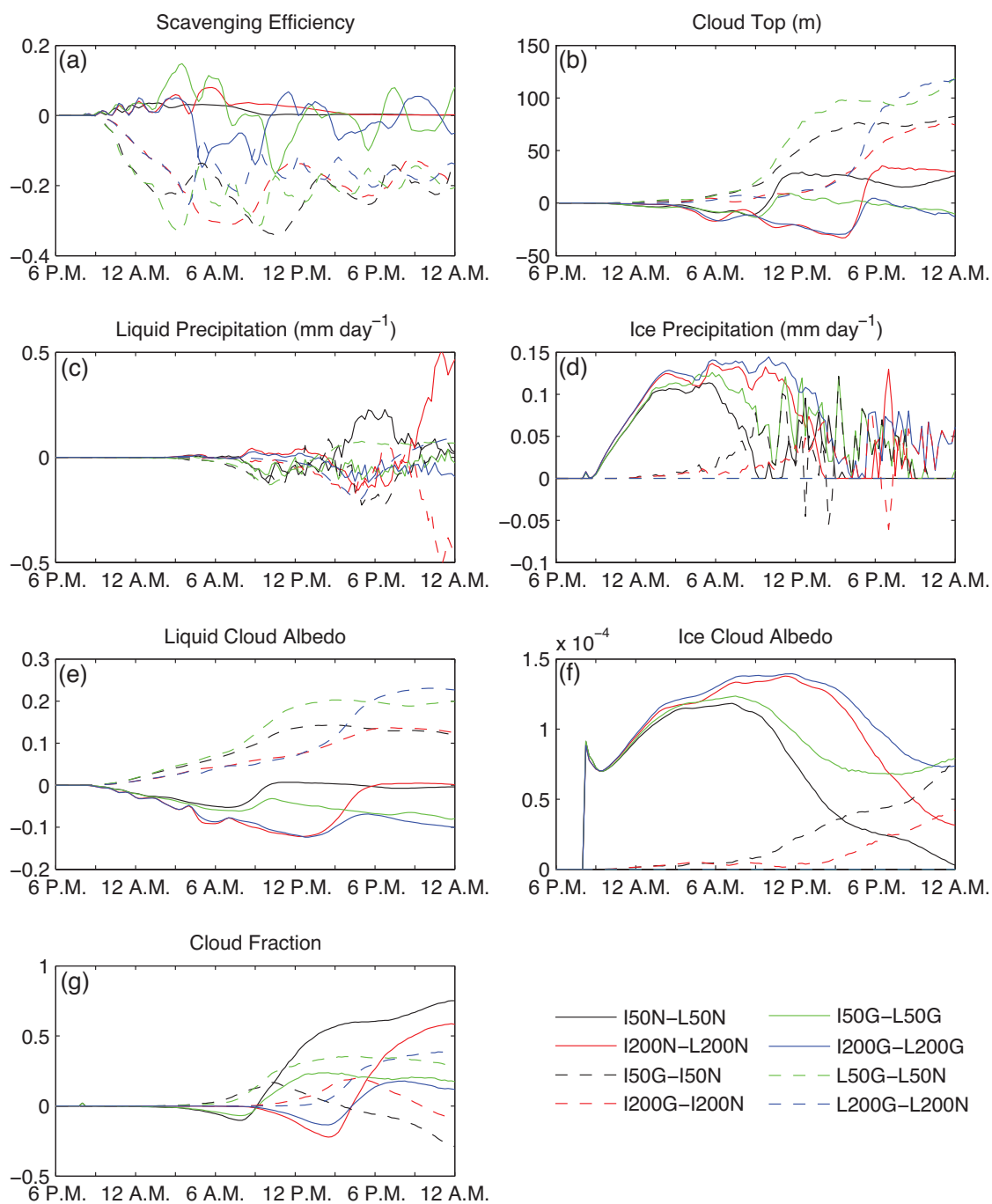


Figure 4: Same as Figure 2 but showing differences between injection vs no injection (dashed lines) and inclusion of ice processes vs exclusion of ice processes (solid lines).

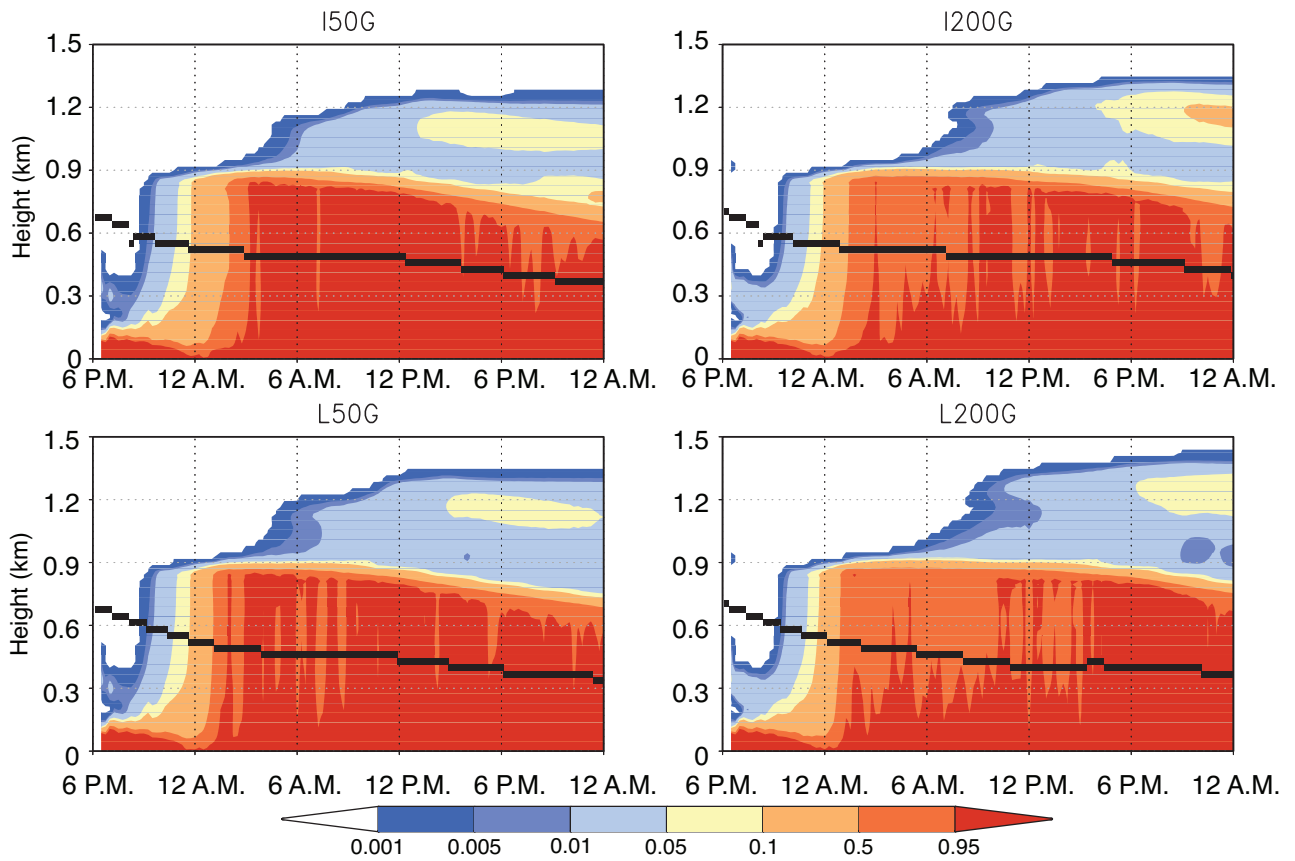


Figure 5: Transport efficiency (Equation 2) for all injection simulations (Table 2). All values shown are calculated only from passive tracers. Thick black line indicates the base of the cloud.

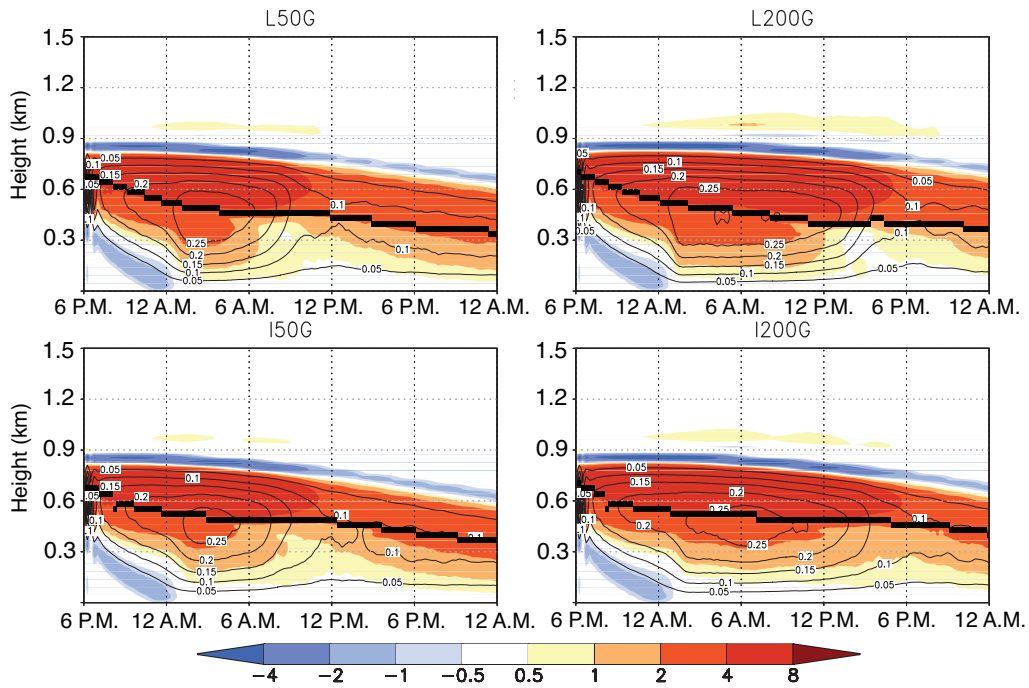


Figure 6: Buoyancy flux source of TKE (shading; $\text{cm}^2 \text{s}^{-3}$) and vertical velocity variance (contours; $\text{m}^2 \text{s}^{-2}$) for each experiment as a function of time (x -axis) and height (y -axis). Buoyancy flux is calculated as $(g/\overline{\theta_v})\overline{w'\theta'_v}$, where g is acceleration due to gravity, θ_v is virtual potential temperature, w is vertical velocity, a bar indicates the domain mean, and a prime indicates the perturbation from the mean. Vertical velocity variance is calculated as $\overline{w'w'}$.

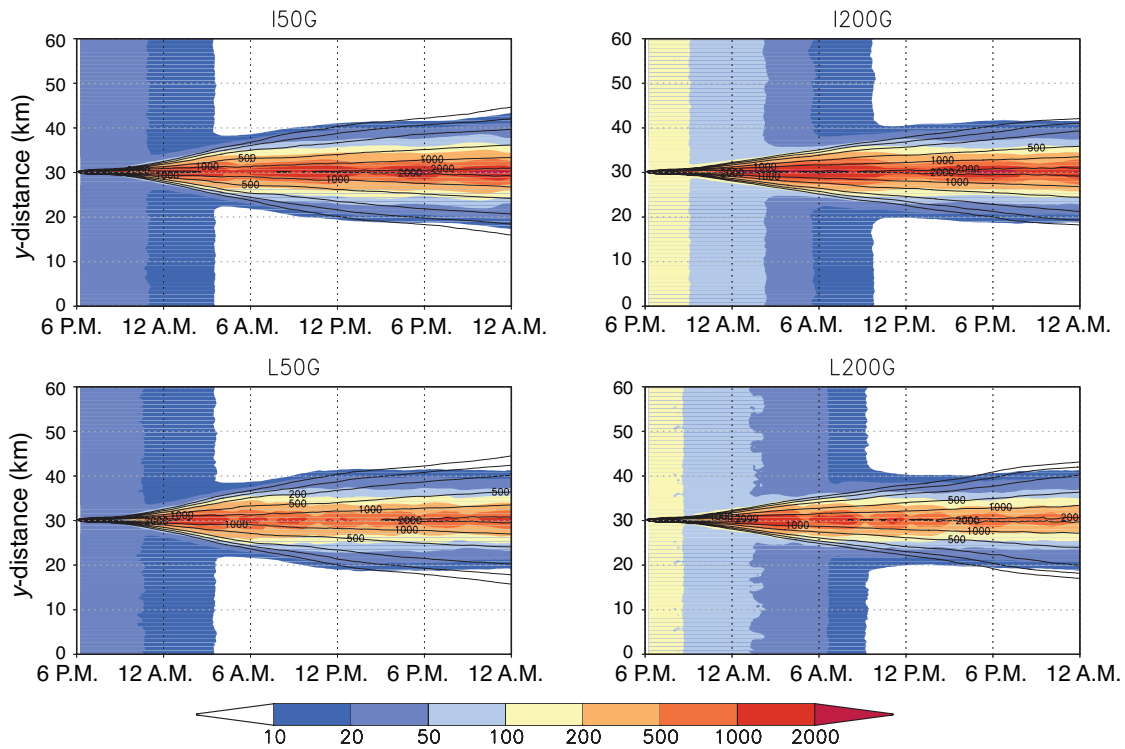


Figure 7: Shading shows N_T (CDNC plus interstitial CCN), and contours show N_P minus the background CCN (cm^{-3} ; See Section 3.1). x -axis indicates time, and y -axis indicates distance in the y direction (km). N_T values are averages in the x and z directions over all grid boxes containing cloud, and N_P values are averages in the x and z directions over all grid boxes in the domain. Only injection simulations are shown, as behavior of no-injection simulations can be inferred from values away from the center of the domain. Contours are placed at 50, 100, 200, 500, 1000, and 2000 cm^{-3} .

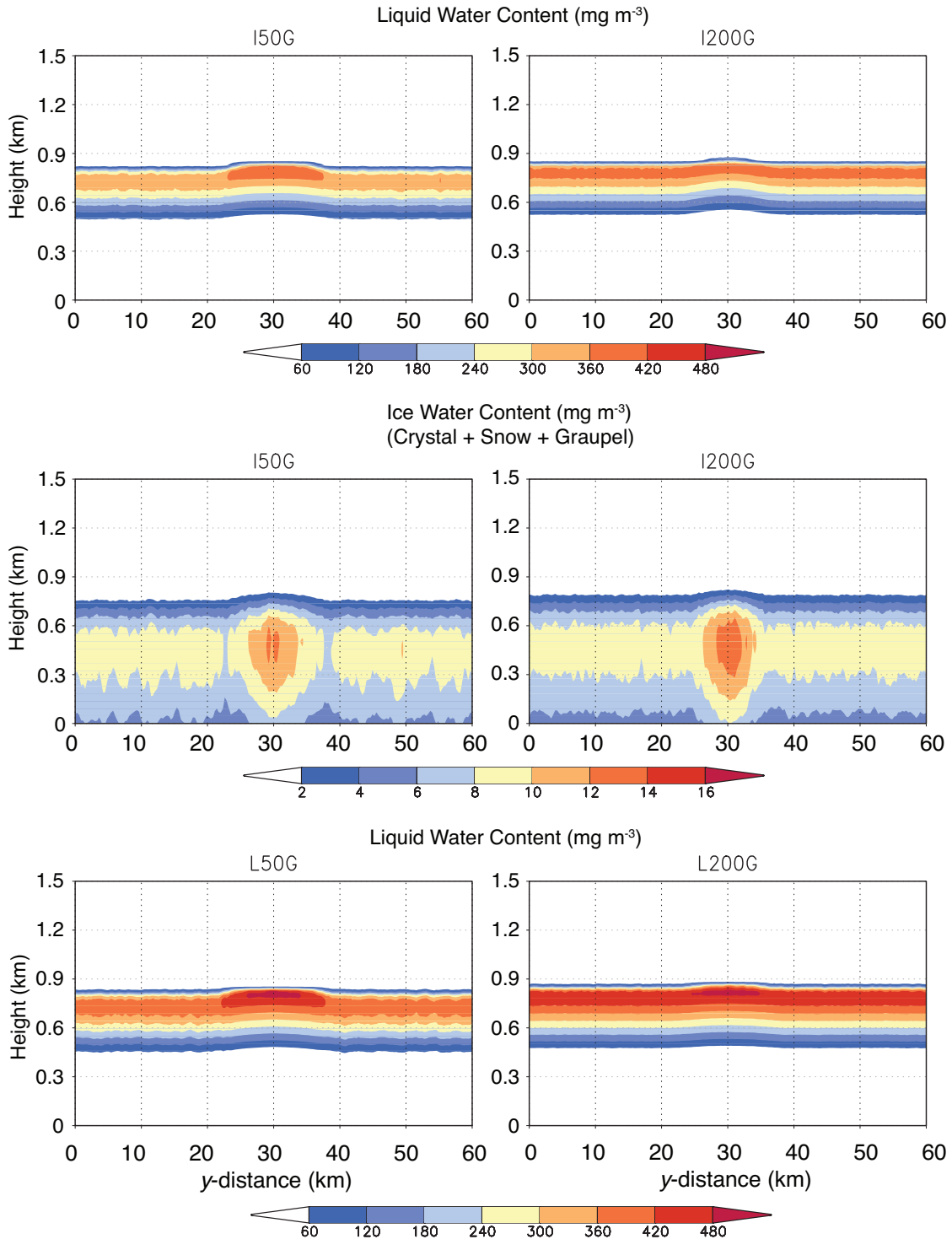


Figure 8: Liquid and ice water content after 12 hours of simulation (6 a.m. local time). Ice water content consists of ice crystals, snow, and graupel. x -axis indicates horizontal distance (km) in the y -direction, and y -axis indicates height (km).

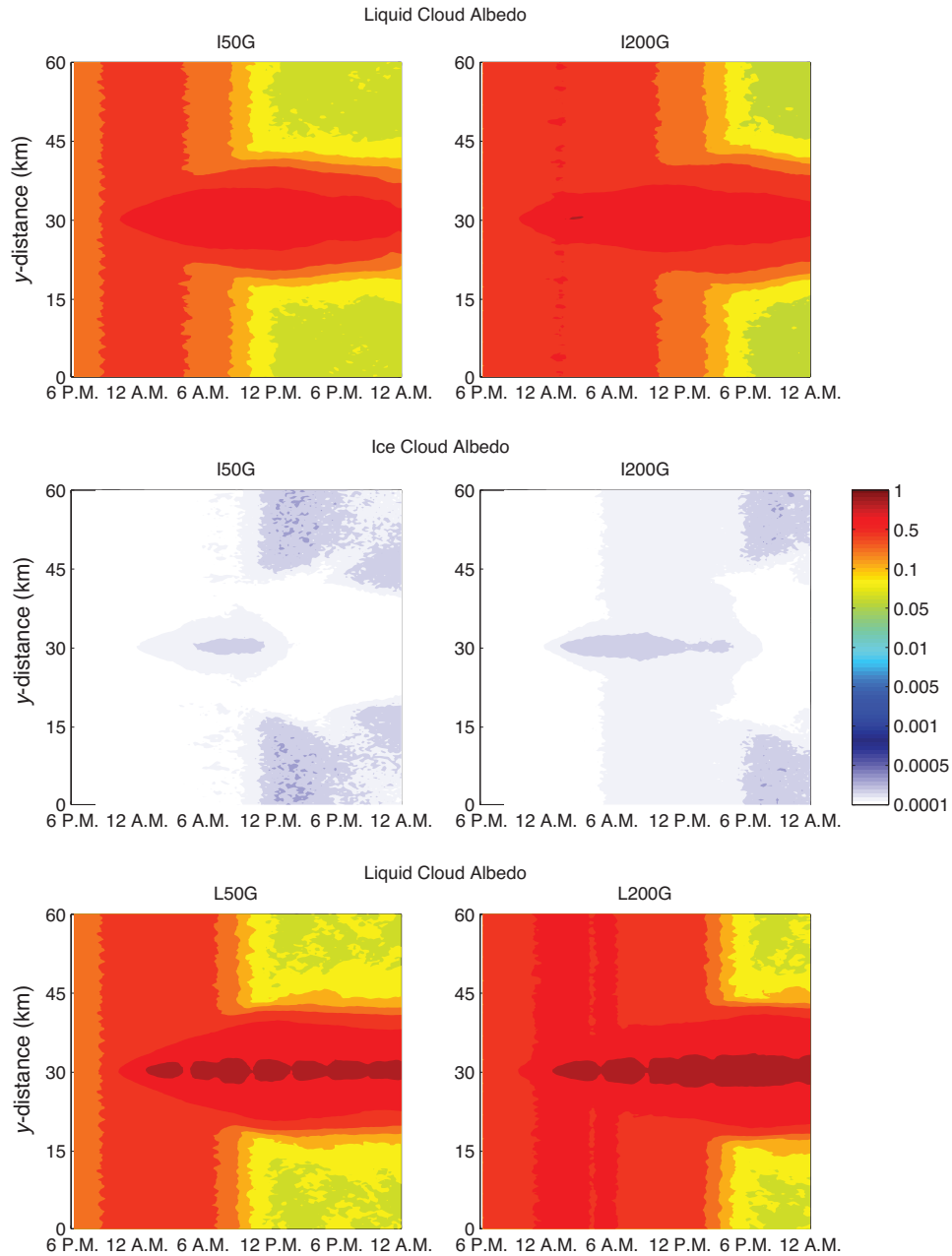


Figure 9: Cloud albedo (liquid or ice) for each injection simulation as a function of time (x -axis) and y -dimension (y -axis). All values are averaged in the x direction and show values for cloud only, not the entire domain. y -axis indicates horizontal distance and has units of km. Only injection simulations are shown, as behavior of no-injection simulations can be inferred from values away from the center of the domain. Ice cloud albedo has no values for the first two hours, as ice processes were not included during this time period (Section 2.3).

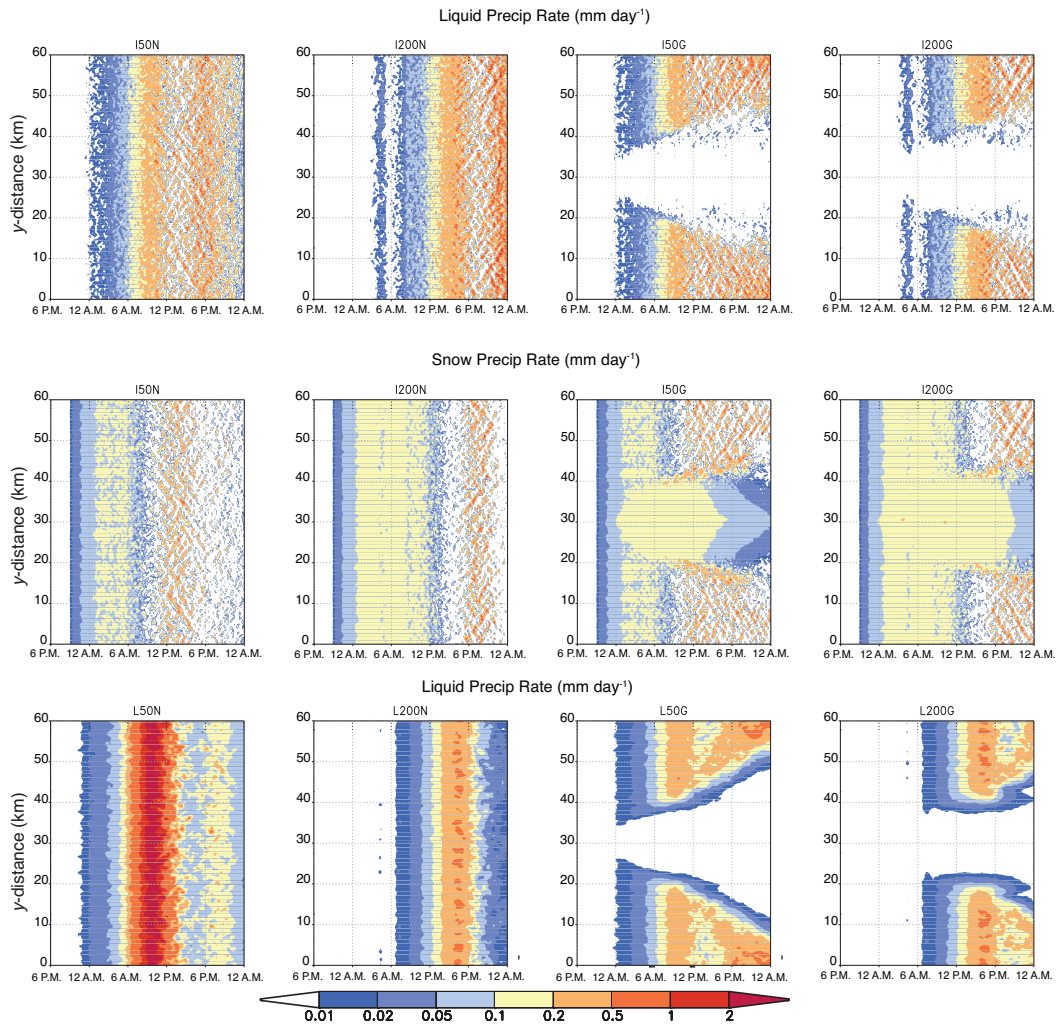


Figure 10: Precipitation rate (rain and snow; mm day^{-1}) for all simulations. x -axis indicates time, and y -axis indicates distance in the y -direction (km). All values are averaged in the x direction.

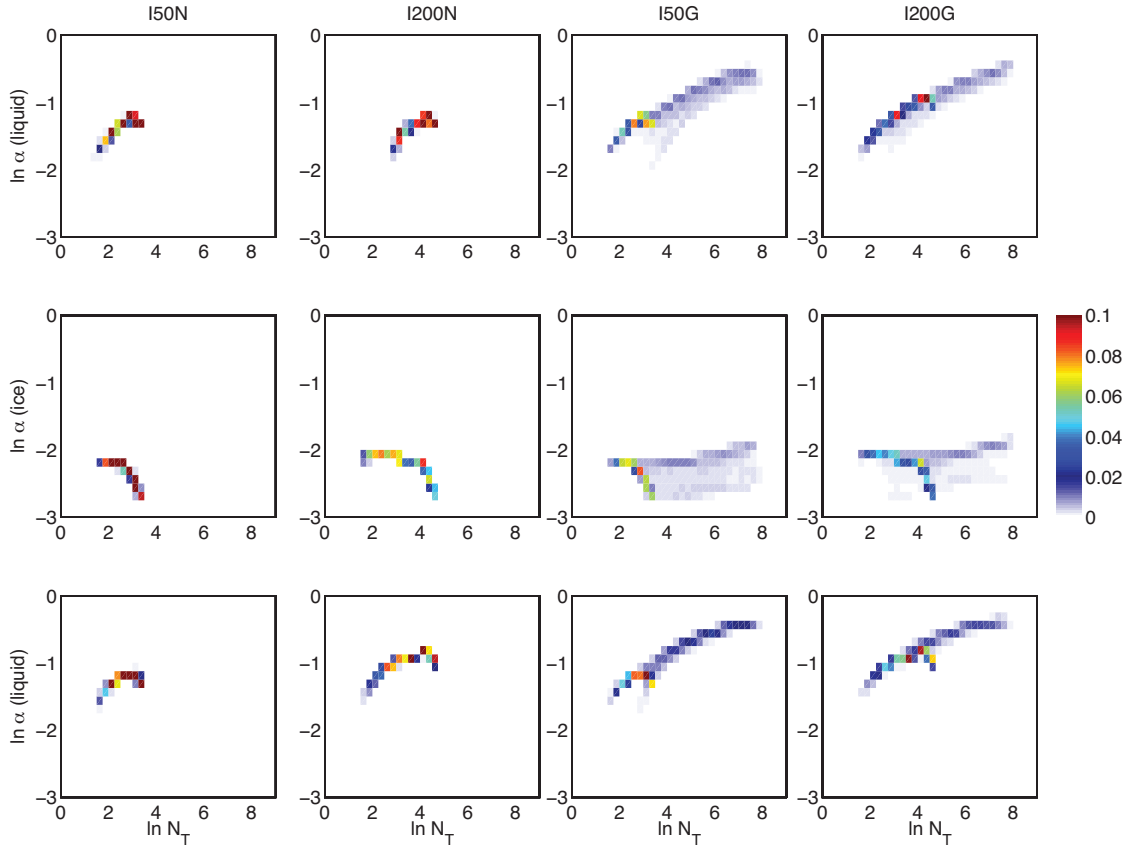


Figure 11: Joint histogram of CDNC plus interstitial CCN (N_T) and cloud albedo (α) for each simulation. Values show frequency of occurrence of each binned combination of N_T and α . Each N_T value (See Section 3.1) indicates an average in the x and z directions over all grid boxes containing clouds. Each α value indicates an average in the x direction over all columns containing clouds (liquid or ice, reported separately). Susceptibility is defined as $d \ln \alpha / d \ln N_T$ (Equation 10) and can be inferred from the joint histogram. Histograms show results for all times after the first three hours of simulation to allow the cloud layer and ice processes to fully develop.